

SIMULATION AND MODELING OF FLOW FIELD AROUND A HORIZONTAL
AXIS WIND TURBINE (HAWT) USING RANS METHOD

By

Armen Sargsyan

A Thesis Submitted to the Faculty of

The College of Engineering and Computer Science

in Partial Fulfillment of the Requirements for the Degree of

Master of Science

Florida Atlantic University

Boca Raton, Florida

December 2010

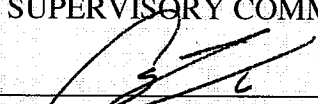
SIMULATION AND MODELING OF FLOW FIELD AROUND A HORIZONTAL
AXIS WIND TURBINE (HAWT) USING RANS METHOD

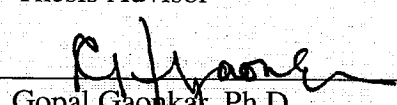
By

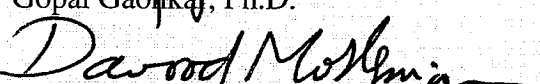
Armen Sargsyan

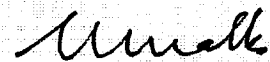
This thesis was prepared under the direction of the candidate's thesis advisor, Dr. Chaouki Ghenai, Department of Ocean and Mechanical Engineering, and has been approved by the members of his supervisory committee. It was submitted to the faculty of the College of Engineering and Computer Science and was accepted in partial fulfillment of the requirements for the degree of Master of Science.

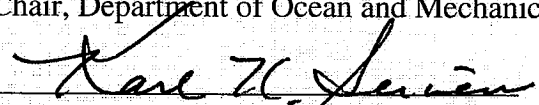
SUPERVISORY COMMITTEE:

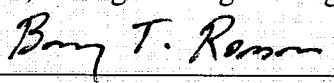

Chaouki Ghenai, Ph.D.
Thesis Advisor


Gopal Gaonkar, Ph.D.


Davood Moslemian, Ph.D.


Mohammad Ilyas, Ph.D.
Chair, Department of Ocean and Mechanical Engineering


Karl K. Stevens, Ph.D., P.E.
Dean, College of Engineering and Computer Science


Barry T. Rosson, Ph.D.
Dean, Graduate College

November 4, 2010
Date

ACKNOWLEDGEMENTS

I would like to thank my advisor Dr. Chaouki Ghenai for his hard work and support in development of the needed resources for this thesis. I owe to him an interest to Computational Fluid Dynamics and wind energy. He gave me a lot of helpful suggestions and has held valuable discussions around the subject of my thesis. Thanks for his patience and time.

I would like to express my deepest gratitude to Dr. G. Gaonkar and Dr. D. Moslemian, for their advices and contributions.

Also, I would like to thank my graduate colleague Zaqie Reza who helped me reviewing this thesis.

I wish to express special thanks to my mother for her unconditional support and love throughout my life.

Finally, I am grateful to my family, my wife Jasmine, my kids Elizabeth and Jacob for their patience and understanding, which made this effort possible.

ABSTRACT

Author: Armen Sargsyan

Title: Simulation and Modeling of Flow Field around a Horizontal Axis Wind Turbine (HAWT) using RANS Method

Institution: Florida Atlantic University

Dissertation Advisor: Dr. Chaouki Ghenai, Ph.D.

Degree: Master of Science

Year: 2010

The principal objective of the proposed CFD analysis is to investigate the flow field around a horizontal axis wind turbine rotor and calculate the turbine's power. A full three dimensional computational fluid dynamics method based on Reynolds Averaged Navier Stokes approach was used in this study. The wind turbine has three blades and a rotor diameter of six meters. One third of the wind turbine rotor was modeled by means of 120° periodicity in a moving reference frame system. The power coefficient curve obtained from the CFD results is compared with experimental data obtained by NREL Phase VI rotor experiment. The numerical result for the power coefficient curve shows close agreement with the experimental data. The simulation results include the velocity distribution, pressure distribution along the flow direction, turbulent wake behind the wind turbine, and the turbine's power. The discussion will also include the effect of wind speed on turbine's power.

SIMULATION AND MODELING OF FLOW FIELD AROUND A HORIZONTAL AXIS WIND TURBINE (HAWT) USING RANS METHOD

LIST OF FIGURES	vii
LIST OF TABLES	ix
1. INTRODUCTION	1
1.1 World Wind Energy	1
1.2 Motivation	2
1.3 Background to Wind Turbine Aerodynamics: Literature Review	3
1.4 Objectives of the Thesis	5
2. AERODYNAMICS OF THE WIND TURBINE	7
2.1 Basic definitions of wind turbines	7
2.2 Rotating Wake Effect	10
2.3 Airfoil Characteristics	13
2.4 Forces acting on an airfoil section	14
3. COMPUTATIONAL FLUID DYNAMICS (CFD)	16
3.1 CFD Principles and Advantages	16
3.2 CFD Code	17
3.2.1 Preprocessor	17
3.2.2 Solver	18
3.2.3 Postprocessor	18
3.3 ANSYS Fluent CFD	19
3.4 Numerical Solvers	20
3.4.1 The Pressure-Based Solver	20
3.4.2 Density-Based Solver	23
4. GOVERNING EQUATIONS	24
4.1 Conservation Equations	24
4.1.1 Continuity Equation	24
4.1.2 Conservation of Momentum Equation	25
4.2 Reynolds Averaged Navier Stokes (RANS) Equations	25
4.3 Turbulence Modeling	26
4.4 Effect of Walls on Turbulent Flows	28
4.4.1 Inner layer	30
4.4.2 Outer layer	31
4.4.3 Overlap Layer	32

4.5	Wall Functions vs. Near-Wall Modeling	33
4.6	Model Selection.	34
4.6.1	Issues with $k-\omega$ SST model	35
4.6.2	$k-\varepsilon$ Turbulent Model.....	36
4.7	Modeling Flows with Rotating Reference Frames	38
4.7.1	Relative Velocity Formulation and MRF.....	38
4.8	Boundary Conditions (BC).....	40
4.9	Modeled Blade.....	42
5.	MESH GENERATION	45
5.1	Structured Grid Methods.....	45
5.2	Unstructured Grid Methods.....	46
5.3	Hybrid Grid Methods	47
5.4	Mesh Quality	48
5.5	Computational Grid and Domain.....	51
6.	VALIDATION OF CFD MODEL RESULTS.....	55
6.1	NREL Phase VI Experiment	55
6.2	CFD vs. Experiment.....	57
6.2.1	Calculation of Efficiency C_p	58
7.	RESULTS AND DISCUSSIONS	61
7.1	Flow Visualization	61
7.2	Parametric Studies	80
	CONCLUSION	84
	REFERENCES.....	90

LIST OF FIGURES

Figure 1. World total Installed Capacity by the end of 2009	2
Figure 2. Flow velocity diagram at an annulus in HAWT rotor disk	11
Figure 3. Power coefficient curve with and without wake rotation	12
Figure 4. C_p vs. λ curve for actual wind turbine	13
Figure 5. Airfoil section	14
Figure 6. Forces acting on airfoil	14
Figure 7. Finite-volume representations in Cartesian coordinates: a) 2D b) 3D	19
Figure 8. Near Wall region profile shape	29
Figure 9. Subdivisions of near wall region	30
Figure 10. Wall function approach v/s Enhanced wall treatment	33
Figure 11. Sensitivity to the distance of the first point to the wall, (y^+)	36
Figure 12. Coordinate system for moving reference frame	39
Figure 13. 2-D views of the turbine and the applied boundary conditions	42
Figure 14. Modeled blade (Rhinceros 4.0).	44
Figure 15. Aspect ratio= A/B	50
Figure 16. Graphical visualization of computational domain (periodic)	51
Figure 17. Computational Domain Dimensions	52
Figure 18. Blade and the hub embedded in tetra mesh	53
Figure 19. Mesh of the root of blade and hub section	53
Figure 20. Mesh cut plane at blade	54
Figure 21. y^+ resolutions at prism layers	54
Figure 22. Wind Turbine Testing in NASA (10 m in diameter)	56

Figure 23. NASA-Ames 80' x 120' Wind Tunnel	56
Figure 24. NREL Phase VI rotor blade	57
Figure 25. C_p versus λ comparison plot CFD vs. experiment	59
Figure 26. Torque vs. wind speed	60
Figure 27. Axial velocity contours at different x/D locations for $TSR=7$	58
Figure 28. Axial velocity distributions along the flow direction	65
Figure 29. Axial velocity plots along the radial lines.....	68
Figure 30. Radial velocity plots at different x/D locations.....	70
Figure 31. Tangential velocity contours at different x/D locations.....	71
Figure 32. Tangential velocities along the blade.....	74
Figure 33. Axial velocities along the x-direction.....	74
Figure 34. Radial velocities along the x- direction	75
Figure 35. Pathlines colored by velocity magnitude	76
Figure 36. Static pressure distributions along the flow direction.....	76
Figure 37. Turbulent viscosity contours, $TSR=7$, $V_0=10$ m/s.....	77
Figure 38. Turbulence intensity contours, $TSR = 7$, $V_0 =10$ m/s.....	78
Figure 39. Turbulent viscosity plots at different x/D locations	79
Figure 40. Turbulent intensity plots at different x/D locations.....	79
Figure 41. Power outputs vs. wind speed, $\omega=7.53$ rad/s.....	81
Figure 42. Power coefficient (efficiency) vs. wind speed, $\omega=7.53$ rad/s.....	82
Figure 43. Mechanical power at different TSR , $V_0=10$ m/s	83
Figure 44. Control Volume for the idealized actuator-disk analysis.....	86

LIST OF TABLES

Table 1. Turbine's particulars	43
Table 2. Foil Section Characteristics	44
Table 3. Power output at different wind speeds	80
Table 4. Turbine's characteristic parameters at different TSR, $V_0=10$ m/s.....	82

CHAPTER

1. INTRODUCTION

1.1 World Wind Energy

There are two common sources of energy: renewable and non-renewable. Till now, most energy demand is covered by non-renewable energies like petroleum, coal and natural gas, generating electrical power by burning technologies and cannot be renewed. In the renewable energy sector, wind power represents most mature technology. In March of 2007, the European Council endorsed a binding target to satisfy 20% of the EU's energy consumption with renewable energy sources by 2020 [1]. Meanwhile, in 2008, U.S. Department of Energy (DOE) published a report that examines the technical feasibility of using wind energy to generate 20% of nation's electricity demand by 2030 [2]. In the last 25 years the global wind energy capacity had been increasing rapidly and at the end of 2009 reached 159,213MW. Wind power showed a growth rate of 31.7 %, the highest rate since 2001. Capacity doubles every three years. Figure 1 shows the total installed wind capacity worldwide.



Figure 1. World total Installed Capacity by the end of 2009

(Data source: WWEA, www.wwea.org)

Based on accelerated development and further improved policies, World Wind Energy Association (WWEA) predicted total wind capacity to exceed 200,000 Megawatts of energy within the year 2010 and increased its predictions for global wind capacity to reach 1,900,000 Megawatts as possible by the year 2020. The wind sector employed 550,000 persons worldwide. In the year 2012, the wind industry is expected for the first time to offer 1 million jobs [1, 2].

1.2 Motivation

Wind energy represents a low density source of power. Maximizing the efficiency of converting wind energy into mechanical form of energy has greatest importance of making wind power economically feasible. The knowledge and understanding of rotor aerodynamics, the design of blades shapes improves the overall performance of the modern turbines. Wind turbine technology is based on force distributions on the blades of

turbine's rotor, resulting mechanical torque at the shaft. The shaft transfers the torque from the blades to the generator. In modern wind turbines aerodynamic driving force is mainly the lift force rather than drag force like it was in ancient sailing ships. Research work conducted in this area has brought to a substantial improvement in the overall efficiency in energy conversion process.

The ability to predict the downstream wakes of the flow field is a significant factor for determining the interactions between turbines. Three approaches are available to analyze the flow around and downstream of wind turbines [3]:

1. Field testing; this provides accurate results but is highly complex and expensive.
2. Analytical and semi-empirical models, which adopt simplified assumptions and are thus not universally reliable.
3. Computational Fluid Dynamics (CFD), which offers the best alternative to direct measurements.

The aim of this thesis is to study the aerodynamics of HAWT by numerically solving governing equations using finite-volume method and Reynolds Averaged Navier-Stokes method.

1.3 Background to Wind Turbine Aerodynamics: Literature Review

A wind turbines performance and rotor characteristics was the subject of investigation for many years. In 1915, Lanchester [21] was first to predict the maximum efficiency of an ideal wind turbine of 59.3%. In 1920 German scientist Betz and Russian scientist

Joukowski, derived this maximum efficiency independently, being unaware of Lanchester's findings. However, the limit is known as Betz limit. The major breakthrough in rotor predictive methods was achieved by Glauert [25], who formulated the Blade Element Momentum (BEM) method in 1935. The method based on momentum balance equations for individual annular streamtubes passing through the rotor. In BEM, the wind turbine blade is divided into separate blade segments and analyzed from a two-dimensional perspective. Today, industrial rotor design codes are still based on BEM [3, 4 and 5]. Aerodynamic modeling of HAWT rotors by means of the conventional engineering methods has reached a point where no further improvement can be expected without a full understanding of the flow physics [6]. Extensive use of numerical studies on all HAWT aerodynamics features, performed on many different levels, ranging from BEM methods integrated by CFD calculations to full 3D Navier-Stokes models became quite popular way to predict performance and characteristics of modern wind turbines. Many authors have used the generalized Actuator Disk Method that represents roughly an extension of BEM method, integrated in an Euler or Navier-Stokes frame [7, 8]. The method describes the forces that are distributed evenly along the azimuthal direction; 3D Navier-Stokes solver has been combined with the so-called Actuator Line Technique, in which the loading is distributed along lines representing the blade forces [4, 5, and 8]. In the few past years, Sankar and co-workers [9, 10, and 11] developed a hybrid Navier-Stokes/Full-Potential/Free Wake Method, mainly for predicting 3D viscous flow over helicopter rotors. The method has recently been extended to deal with the HAWT flow fields. The computational domain is divided in different regions, each one solved by the proper approach: Navier-Stokes solution near the blades, potential flow representation on

outer field and a collection of vortex methods for modeling the vorticity field. Full three-dimensional computations employing the Reynolds-averaged Navier-Stokes (RANS) equations have been carried out by Duque [12], Ekaterinaris [13], Sørensen and Michelsen [14]. Risø and Denmark Technical University performed several numerical investigations on HAWT using their Navier-Stokes solver EllipSys 2D/3D, dealing with overall performances and design of rotors and blade sections [4, 15, and 16], extreme operation conditions [17] and tip shape [18]. In 2008, Mandas, et al. [19] at the University of Cagliari in Italy used the commercial code Fluent to perform a detailed analysis of HAWT flow. The steady flow field around an isolated rotor of a middle-sized HAWT is predicted in a non-inertial reference frame, using both the Spalart-Allmaras [27] and the Menter's $k-\omega$ SST [20] turbulence models for closure, and specifying a constant axial wind velocity at the inlet. Similarly, in this thesis, the 3D behavior of the wake, the upstream and downstream flow will be investigated by using finite – volume method and Reynolds Averaged Navier-Stokes approach.

1.4 Objectives of the Thesis

The main objective of this thesis is to analyze the flow field around the horizontal axis wind turbine by numerically solving the governing equations using a finite-volume method and Reynolds's Averaged Navier-Stokes (RANS) approach. Upstream and downstream wake visualization in terms of x , y and z - velocities are in the scope of the thesis. Also, tangential velocity at the tip of the blade will be plotted and compared with

theoretical results. The other objective of the thesis is to determine the efficiency and power extracted by wind turbines.

The project is structured as follows:

- Modeling the one-third of the wind turbine rotor by means of 120° periodicity. Select the geometry of the blade shape by BEM designing techniques.
- Create computational domain for flow field analysis and generate high quality mesh.
- Select the turbulence model for simulation of the flow field.
- Validate the model with available experimental data.
- Flow visualization and wake analysis.
- Calculate the power extracted by the turbine.
- Study the effect of wind speed on turbine's power.

CHAPTER

2. AERODYNAMICS OF THE WIND TURBINE

2.1 Basic definitions of wind turbines

The following parameters were used in calculations of turbine's power coefficient:

Tip speed ratio

Tip speed ratio (also called TSR or λ) is defined by ratio between the tip speed (tangential velocity) and the undisturbed wind speed entering the turbine.

$$\lambda = \frac{\Omega r}{V_{\infty}} \quad [2.1.1]$$

Where, Ω is the angular velocity, r is the radius of the rotor and V_{∞} the undisturbed wind speed. This is a dimensionless quantity and it represents a very important turbine parameter. Typical values of tip speed ratio for the modern turbines are 6 to 8.

Induction factor

The fractional decrease in wind velocity between the free stream and rotor plane can be expressed in terms of an axial induction factor, a :

$$a = \frac{V_0 - V}{V_0} \quad [2.1.2]$$

Where, V is the velocity at the disk (see Appendix A) and it is defined by

$$V = \frac{1}{2}(V_0 + V_3) \quad [2.1.3]$$

V_0 and V_3 are free stream and downstream velocities respectively.

The amount of axial induction factor determines the amount of power extracted by turbine.

Power coefficient

Intercepting the greatest practical cross-sectional area of wind creates the opportunity to extract the greatest amount of energy. The practical efficiency of a wind turbine is usually represented by power coefficient C_p , defined as that the power extracted by rotor to power available in the wind.

$$C_p = \frac{P}{\frac{1}{2}\rho AV^3} = \frac{\text{Power Extracted by Rotor}}{\text{Power Available in the Wind}} \quad [2.1.4]$$

The power coefficient C_p , defined as extracted power over the total available power can be similarly defined in terms of axial induction factor a as:

$$C_p = 4a(1-a)^2 \quad [2.1.5]$$

Lanchester–Betz–Joukowski limit [21] shows that the actual turbine cannot extract more than 59.3% of the power in an undisturbed tube of air of the same area. In practice, the fraction of power extracted will always be less because of mechanical imperfections. A

good fraction is 35-40% of the power in the wind under optimum conditions, although fractions as high as 50% have been claimed [19]. A turbine which extracts 40 percent of the power in the wind is extracting about two-thirds of the amount that would be extracted by an ideal turbine

$$C_{p_{\max}} = C_{p, \text{Betz}} = \frac{16}{27} = 0.593 \quad [2.1.6]$$

Maximum C_p is decreased by:

1. Wake rotation behind (downstream) of the rotor
2. A non-uniform pressure distribution in the turbine plane
3. Tip losses and number of blades
4. Aerodynamic drag

Wake rotation has high impact on the efficiency of the turbine and it is much related to this thesis. An overview of this phenomenon will be presented in section 2.2.

Turbines Power

Wind power is proportional to the cube of wind's velocity. This relationship is presented mathematically by the following equation:

$$P = \frac{1}{2} \rho A V^3 \quad [2.1.7]$$

Where,

ρ - Air density (typically 2.7 lb/in³ or 1.2 kg/m³ at sea level and 59°F/15°C) [kg/m³]

P – Wind power	[W]
A – Cross-sectional area (swept area) of the wind being measured	[m ²]
V- Mean velocity of the wind measured at within cross-section	[m/s]

2.2 Rotating Wake Effect

The impact of the rotating wake can be estimated by extending the Betz analysis to a 2-D model in the radial direction. The flow far upstream is purely axial; however, there is discontinuous jump in angular velocity across the rotor plane because torque is exerted on the rotor. While the flow imparts a torque to the disk, the disk in turn imparts an equal and opposite torque to the flow. Therefore, if the disk rotates with angular velocity Ω , the flow rotates in the opposite direction, say with angular velocity ω . Now, consider an observer moving with the disk with angular velocity Ω . The observer sees that the flow behind the rotor is moving with angular velocity $\Omega - (-\omega)$ or $\Omega + \omega$ in the opposite direction. Two additional expressions are customarily introduced: an angular induction factor, a' , and local tip speed ratio λ_r , defined as:

$$a' = \frac{\omega}{2\Omega} \quad [2.2.1]$$

$$\lambda_r = \frac{\Omega r}{V_0} = \lambda \frac{r}{R} \quad [2.2.2]$$

Glauert [25] derived the expression for the pressure, $p_2 - p_3$, by applying Bernoulli's energy equation [26] with respect to observer, before and after the disk.

$$p_2 - p_3 = \rho \left(\Omega + \frac{\omega}{2} \right) \omega r^2 \quad [2.2.3]$$

Therefore, differential thrust and torque on annular disk, exerted in terms of the induction factors are:

$$dT = \rho \Omega^2 r^2 4a'(1+a')\pi r dr \quad [2.2.4]$$

$$dT_0 = \rho V_0 \Omega r^2 4a'(1-a)\pi r dr \quad [2.2.5]$$

The Figure 2 illustrates the rotational wake influence on velocity vectors in the plane of turbine's rotor. Note that when wake rotation is included in the analysis, the induced velocity at the rotor consists of not only the axial component, aU , but also a component in the rotor plane $r\Omega a'$ [47].

aU here represents induced velocity.

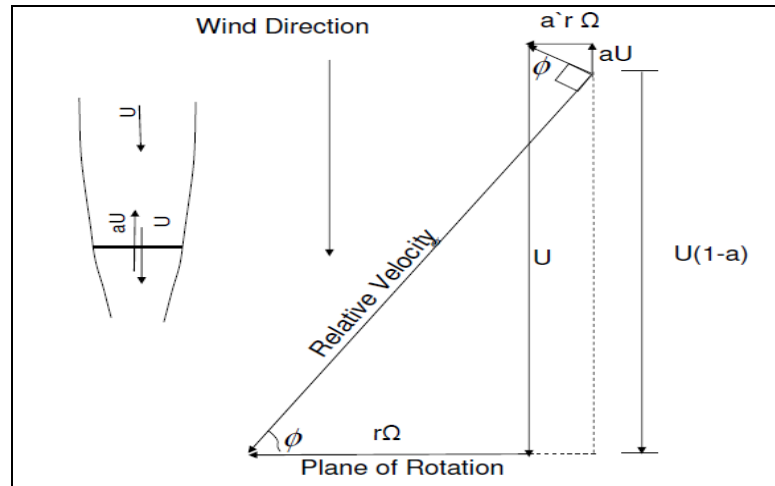


Figure 2. Flow velocity diagram at an annulus in HAWT rotor disk

Also, it can be shown for an ideal turbine the two induction factors are related and defined as:

$$a' = \frac{1}{2} \left(\sqrt{1 + \frac{4}{\lambda_r^2} a(1-a)} - 1 \right) \quad [2.2.6]$$

Figure 3 depicts the theoretical maximum power coefficient as a function of tip speed ratio with and without wake rotation effect [8].

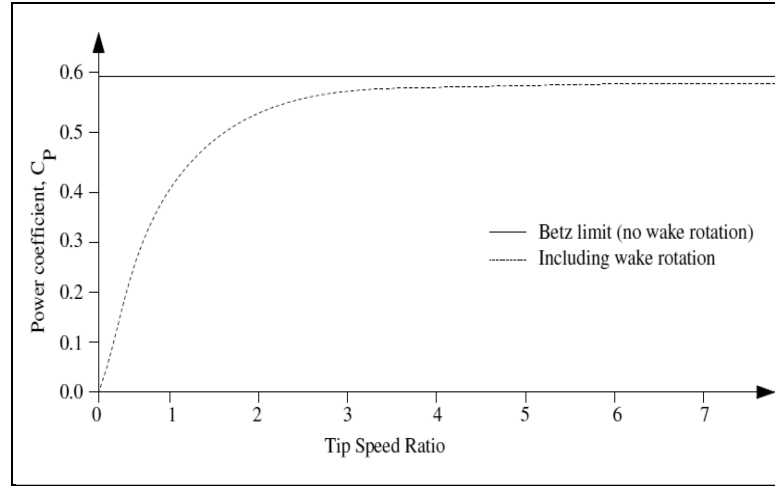


Figure 3. Power coefficient curve with and without wake rotation

Power coefficient including wake rotation can be expressed as a function of local tip speed ratio and angular induction factor:

$$C_p = \frac{8}{\lambda^2} \int_0^{\lambda} \frac{8}{\lambda^2} a'(1-a) \lambda_r^3 d\lambda_r \quad [2.2.7]$$

Typical turbine performance from real devices is presented in the Figure 4 bellow which depicts the power coefficient plotted against tip speed ratio, λ [22].

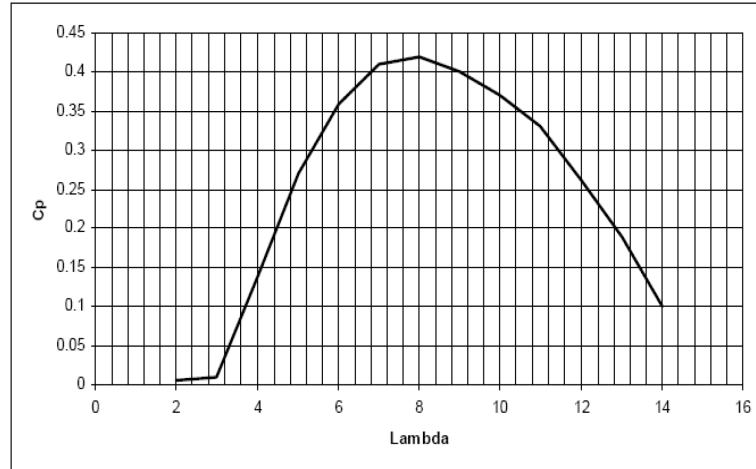


Figure 4. C_p vs. λ curve for actual wind turbine

2.3 Airfoil Characteristics

A number of terms are used to characterize an airfoil. The mean camber line is the locus of a point midway between upper and lower surfaces of the airfoil. The most forward and rearward ends of this locus line are the leading edge and the trailing edge respectively. The line connecting the leading edge and the trailing edge is the chord line and the distance between the two edges is called chord, c . Camber is the distance from the mean camber line to the chord line, measured perpendicular to the chord line. The thickness t , is the distance between the upper and lower surfaces, also measured perpendicular to the chord line. The angle of attack, α , is the angle between the relative water velocity and the chord line. A graphical representation of an airfoil section is shown in Figure 5.

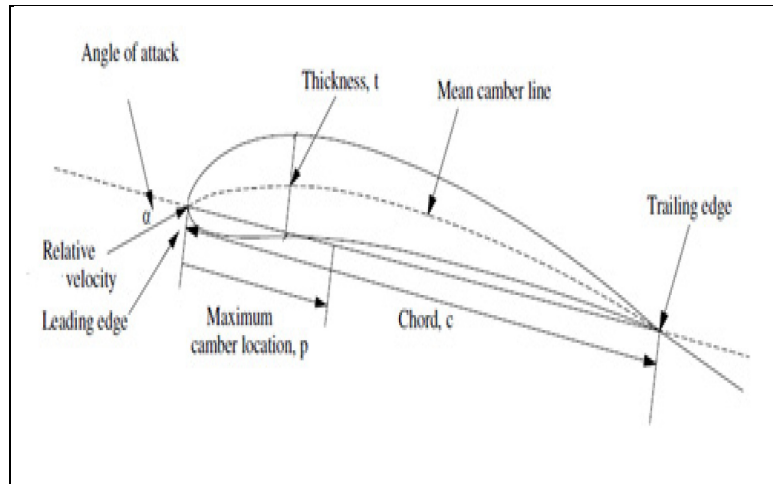


Figure 5. Airfoil section

2.4 Forces acting on an airfoil section

When an imminent flow encounters an airfoil section, forces act on it. The forces can be resolved as normal force, F_N (as shown in Figure 6), along the flow direction and thrust force F_T , orthogonal to it. Alternatively they can be resolved into lift force F_L , normal to the relative velocity of the flow and drag forces F_D , along the flow.

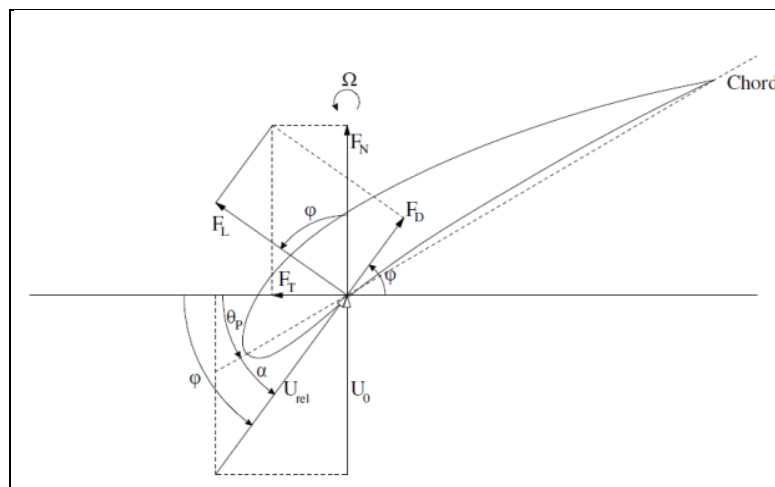


Figure 6. Forces acting on airfoil

Where,

θ_p	-	Pitch angle	Ω	-	Rotational velocity
α	-	Angle of attack	F_L	-	Lift force
φ	-	Angle of relative flow	F_D	-	Drag force
U_0	-	Inflow velocity	F_N	-	Normal force
U_{rel}	-	Relative velocity	F_T	-	Thrust force

CHAPTER

3. COMPUTATIONAL FLUID DYNAMICS (CFD)

3.1 CFD Principles and Advantages

Computational Fluid Dynamics can be explained as numerical solution of the differential governing equations of fluid flows with the help of computers. CFD solvers are based on solution to any of the following three fundamental principles:

- Conservation of mass
- Newton's second law (conservation of momentum)
- Conservation of energy

These principles can be expressed in terms of mathematical equations, mostly in integral and partial differential equation forms. CFD is a tool to replace these equations with discretised algebraic equations, which in turn are solved in forms of numbers; hence the end product of simulation is a collection of numbers [30].

Computational fluid dynamics results are analogous to wind tunnel results obtained in laboratories: they both provide the set of data for a given flow configurations at different conditions like laminar or turbulent, steady or unsteady. However, unlike the wind tunnel, associated with high cost and maintenance, CFD results are more affordable.

A number of valuable advantages are achieved by following CFD approach applied to fluid dynamic problems:

- CFD is faster and cheaper. Significant reduction of time and cost for solving the problems compared to the traditional approaches.
- Wind tunnels are limited in size, therefore full size analysis are hard to perform for a large systems (e.g., world's largest wind turbine ENERCON E-126 has 126m diameter rotor and it is about 200m high). A CFD study is a favorable choice in this case.
- CFD provides a detailed solution, allowing effective analysis of the model at every location at any time instant.
- With the latest advancements in technologies, turbulent models and solution schemes, numerical models of the physical problems have good accuracy and reliability.
- In most cases (other than turbines) the prediction of fluid flows does not require powerful workstations and sometimes personal computers might be sufficient.

3.2 CFD Code

Most commercial CFD codes are divided into three phases: Preprocessor, Solver and Postprocessor. An overview of each phase is presented in the following sections

3.2.1 Preprocessor

In preprocessor phase the physical problem is converted into mathematical model. The computational domain is defined and subdivided into smaller portions called *grid* or *mesh*. Fluid is defined and boundary conditions are set. Since the CFD solution depends locally on number of elements or grid, meshing of the domain and geometry is very

important for achieving accuracy in results. Simply, greater the number of grids greater is the accuracy. Mesh spacing has to be accurately enhanced by putting finer grids near the region of high variable gradients and coarsen where effect of the flow is not much important. Moreover, quality of mesh and type of mesh affects the result in a great scale and therefore a special attention has to be paid to the mesh parameters like skewness or aspect ratio. Effect of mesh quality and type is explained later in chapter.

In preprocessor stage geometry is created, loads and boundary conditions are set.

3.2.2 Solver

The numerical solution algorithm is the core of CFD code. CFD solvers work with the following procedure:

- Modeling the problem unknowns
- Discretising the governing equations for the fluid flows
- Solving the algebraic system of equations.

3.2.3 Postprocessor

Postprocessor includes the analysis of the solution results. The solver outputs the set solution variables in forms of graphs and contours. Domain and grid visualizations, vectorial plots, linear, surface and volume integrals, tracking path-lines, dynamic representations, and animations are parts of the post-processing section.

3.3 ANSYS Fluent CFD

Finite- Volume Approach

The commercial code Fluent solve the governing equations for the conservation of mass and momentum, and (when appropriate) for energy and other scalars, such as turbulence and chemical species. In both cases a control-volume-based technique is used [45, 46].

Discretization steps are as follows:

- Division of domain into discrete control volumes using computational grid.
- Integration of governing equations on the individual control volumes to construct algebraic equations for the discrete dependent variables (unknowns), such as velocities, pressure, temperature, and conserved scalars.
- Linearization of the discretized equations and solution of the resultant linear equation system, to yield updated values of the dependent variables.

Figure 7 bellow, shows the small volume elements around the node in 2D and 3D Cartesian coordinates. It uses a co-located grid, meaning that all flow parameters are stored in the cell-centers. Processes can be easily parallelized on multiple computer nodes.

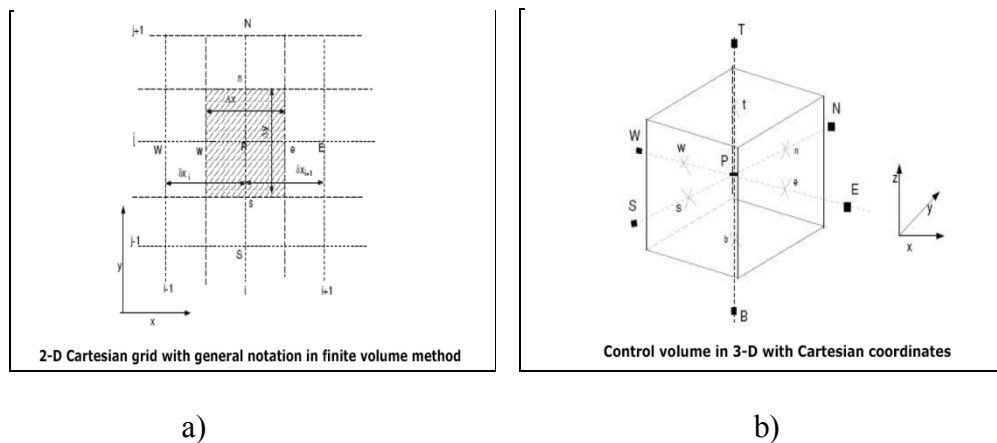


Figure 7. Finite-volume representations in Cartesian coordinates: a) 2D b) 3D

Finite-volume method is conservative: the flux going out through a face of one control volume is equal to the flux coming into the adjacent control volume through the same face.

3.4 Numerical Solvers

Fluent is a commercial 2D/3D mesh solver, which adopts multigrid solution algorithms.

Two numerical solver technologies are available in Fluent:

- Pressure-based solver
- Density-based solver

The first solver was developed for low-speed incompressible flows, whereas the second was created for the high-speed compressible flows solution. In the present study, which involves incompressible flows, the pressure-based approach was preferred. Both approaches are now applicable to a broad range of flows (from incompressible to highly compressible), but the origins of the density-based formulation may give it an accuracy (i.e. shock resolution) advantage over the pressure-based solver for high-speed compressible flows.

3.4.1 The Pressure-Based Solver

The pressure-based solver employs an algorithm which belongs to a general class of methods called the projection method. In the projection method, the constraint of mass conservation (continuity) of the velocity field is achieved by solving a pressure (or pressure correction) equation. The pressure equation is derived from the continuity and the momentum equations in such a way that the velocity field, corrected by the pressure,

satisfies the continuity. Since the governing equations are nonlinear and coupled to one another, the solution process involves iterations wherein the entire set of governing equations is solved repeatedly until the solution converges. [31]

Fluent provides three different solver formulations:

- Segregated
- Coupled implicit
- Coupled explicit

The manner in which the governing equations are linearized may take an "implicit" or "explicit" form with respect to the dependent variable (or set of variables) of interest. By implicit or explicit we mean the following:

- Implicit: For a given variable, the unknown value in each cell is computed using a relation that includes both existing and unknown values from neighboring cells. Therefore each unknown will appear in more than one equation in the system, and these equations must be solved simultaneously to give the unknown quantities.
- Explicit: For a given variable, the unknown value in each cell is computed using a relation that includes only existing values. Therefore each unknown will appear in only one equation in the system and the equations for the unknown value in each cell can be solved one at a time to give the unknown quantities.

All three solver formulations will provide accurate results for a broad range of flows. In some cases one formulation may perform better (i.e., yield a solution more quickly) than others. The segregated pressure-based solver uses a solution algorithm where the governing equations are solved sequentially (i.e. segregated) from one another. The segregated algorithm is memory-efficient, since the discretized equations need only be

stored in the memory one at a time. However, the solution convergence is relatively slow, in as much as the equations are solved in a decoupled manner.

The pressure-based coupled algorithm solves a coupled system of equations comprising the momentum equations and the pressure-based continuity equation. The remaining equations (i.e. scalars) are solved in a decoupled fashion as in the segregated algorithm. Since the momentum and continuity equations are solved in a closely coupled manner, the rate of solution convergence significantly improves when compared to the segregated algorithm. However, the memory requirement increases by 1.5 – 2 times that of the segregated algorithm since the discrete system of all momentum and pressure-based continuity equations needs to be stored in the memory when solving for the velocity and pressure fields (rather than just a single equation, as is the case with the segregated algorithm). By default, FLUENT uses the segregated solver, but for high-speed compressible flows, highly coupled flows with strong body forces (e.g., buoyancy or rotational forces), or flows being solved on very fine meshes, one may want to consider the coupled implicit solver instead. For cases where the use of the coupled implicit solver is desirable, but your machine does not have sufficient memory, the segregated solver or the coupled explicit solver can be used instead. The coupled explicit solver also couples the flow and energy equations, but it requires less memory than the coupled implicit solver. It will, however, usually take longer to reach a converged solution than the coupled implicit solver. For this flow simulation, the coupled explicit pressure-based solver has been used. Scheme is a preferable choice for single phase implementation for steady flows.

3.4.2 Density-Based Solver

The density-based solver solves the governing equations of continuity, momentum, and (where appropriate) energy and species transport simultaneously (i.e., coupled together). Governing equations for additional scalars will be solved afterward and sequentially (i.e., segregated from one another and from the coupled set). In density-based solution method, one can solve the coupled system of equations (continuity, momentum, energy and species equations if available) using, either coupled-explicit formulation or the coupled-implicit formulation. If you choose the implicit option of the density-based solver, each equation in the coupled set of governing equations is linearized implicitly with respect to all dependent variables in the set. In the explicit option of the density-based solver, each equation in the coupled set of governing equations is linearized explicitly.

CHAPTER

4. GOVERNING EQUATIONS

4.1 Conservation Equations

For all flows, CFD numerical methods solve conservation equations for mass and momentum. For flows involving heat transfer or compressibility, an additional equation for energy must be included. Additional transport equations are also solved when the flow is turbulent [32]. In this study, the conservation equations for turbulent flow are presented. The k - ε turbulence modeling will be discussed in later sections.

4.1.1 Continuity Equation.

The general equation for conservation of mass, or continuity equation, can be written as follows:

$$\frac{d\rho}{dt} + \nabla \cdot (\rho \vec{v}) = S_m \quad [4.1.1]$$

Where, ρ is the density of the fluid and \vec{v} is the velocity vector. The source S_m is the mass added to the continuous phase from the dispersed second phase (e.g., due to vaporization of liquid droplets. This term vanishes in our case as there is no change in phase.

4.1.2 Conservation of Momentum Equation

The general equation can be written in the following form:

$$\frac{d}{dt}(\rho \vec{v}) + \nabla \cdot (\rho \vec{v}) = -\nabla p + \nabla \cdot \bar{\bar{\tau}} + \rho \vec{g} + \vec{F} \quad [4.1.2]$$

Where p is the static pressure, and $\rho \vec{g}$ and \vec{F} are the gravitational body force and external body forces (e.g., that arise from the interaction with the dispersed phase), respectively. \vec{F} also contains other model-dependent source terms such as porous-media and user-defined sources.

The stress tensor $\bar{\bar{\tau}}$ is given by

$$\bar{\bar{\tau}} = \mu \left[(\nabla \vec{v} + \nabla \vec{v}^T) - \frac{2}{3} \nabla \cdot \vec{v} I \right] \quad [4.1.3]$$

Where μ is the molecular viscosity and I is the unit tensor.

4.2 Reynolds Averaged Navier Stokes (RANS) Equations

The Reynolds-averaged Navier-Stokes (RANS) equations are time-averaged equations of motion for fluid flow. They are primarily used while dealing with turbulent flows. These equations can be used with approximations based on knowledge of properties of flow turbulence to give approximate average solutions to the Navier-Stokes equations. The equations can be written in Cartesian tensor form as:

$$\frac{d\rho}{dt} + \frac{d}{dx_i}(\rho u_i) = 0 \quad [4.2.1]$$

$$\frac{d}{dt}(\rho u_i) + \frac{d}{dx_i}(\rho u_i u_j) = -\frac{d\rho}{dx_i} + \frac{d}{dx_j} \left[\mu \left(\frac{du_i}{dx_i} + \frac{du_j}{dx_j} - \frac{2}{3} \delta_{ij} \frac{du_i}{dx_j} \right) \right] + \frac{d}{dx_i}(-\rho \overline{u'_i u'_j}) \quad [4.2.2]$$

Equations [4.2.1] and [4.2.2] are called Reynolds-Averaged Navier-Stokes equations, with the velocities and other solution variables now representing ensemble-averaged (or time-averaged) values.

Here u_i , $\overline{u_i}$ and u'_i represent the instantaneous, mean and fluctuating velocity terms.

Given the fluid velocity u_i as a function of position and time, the average fluid velocity

$$u_i = \overline{u_i} + u'_i \quad [4.2.3]$$

The left hand side of the equation [4.2.2] represents the change in mean momentum of fluid element owing to unsteadiness in the mean flow and the convection by the mean flow. This change is balanced by the mean body force, the isotropic stress owing to the mean pressure field, the viscous stresses, and apparent stress $(-\rho \overline{u'_i u'_j})$ owing to the fluctuating velocity field, generally referred to as Reynolds stress. The nonlinear Reynolds stress term requires additional modeling to close the RANS equation for solving, and has led to the creation of many different turbulence models.

4.3 Turbulence Modeling

Turbulent flows are characterized by fluctuating velocity fields. These fluctuations mix transported quantities such as momentum, energy, and species concentration, and cause

the transported quantities to fluctuate as well. Since these fluctuations can be of small scale and high frequency, they are too computationally expensive to simulate directly in practical engineering calculations. Instead, the instantaneous (exact) governing equations can be time-averaged, ensemble-averaged, or otherwise manipulated to remove the small scales, resulting in a modified set of equations that are computationally less expensive to solve. However, the modified equations contain additional unknown variables, and turbulence models are needed to determine these variables in terms of known quantities [32]. Turbulent flows are characterized with high Reynolds number, which defined as:

$$\text{Re} = \frac{\rho V D}{\mu} \quad [4.3.1]$$

Where, D is a characteristic length scale (e.g. the chord length for airfoil sections), V is the undisturbed stream velocity and μ the dynamic viscosity. Basically, this is ratio of the inertial (convective) and viscous forces. When Reynolds number is low (less than 1,200) then flow considered as laminar. When flow becomes turbulent, the fluid motion looks disorganized and particles move in winding path. In this study, for stream velocity of 10 m/s, Reynolds number was calculated to be around 4×10^6 . This confirms that the flow is fully turbulent. To evaluate the flow being either compressible or incompressible, Mach number was calculated and it is found to be less than 0.3, what makes the flow incompressible.

ANSYS Fluent provides the following choices of turbulence models

- Spalart-Allmaras model
- $k-\varepsilon$ models (standard, renormalization-group(RNG), realizable)
- $k-\omega$ models (standard, sheer-stress transport (SST))

- Transition SST models
- Reynolds Stress models (RSM)
- Detached eddy simulation (DES) model
- Large eddy simulation (LES) model

The choice of turbulence model will depend on considerations such as the physics encompassed in the flow, the established practice for a specific class of problem, the level of accuracy required, the available computational resources, and the amount of time available for the simulation. To make the most appropriate choice of model for the application, one needs to understand the capabilities and limitations of the various options [31].

4.4 Effect of Walls on Turbulent Flows

Turbulent flows are significantly affected by the presence of walls. Obviously, the mean velocity field is affected through the no-slip condition that has to be satisfied at the wall. However, the turbulence is also changed by the presence of the wall in non-trivial ways. Very close to the wall, viscous damping reduces the tangential velocity, while kinematic blocking reduces the normal fluctuations. Towards the outer part of near wall region, however, the turbulence is rapidly augmented by the production of turbulence kinetic energy due to the large gradients in mean velocity [31].

The profile shape of the near wall region (see Figure 8) as defined by Ludwig Prandtl and Theodore von Karman can be divided as follows:

- Inner layer
- Outer layer
- Overlap layer

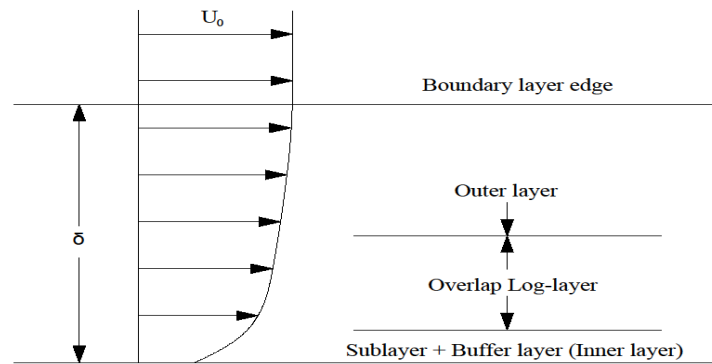


Figure 8. Near Wall region profile shape

Numerous experiments have shown that the near-wall region can be largely subdivided into three layers (see Figure 8). In the innermost layer, called “viscous sublayer”, the flow is almost laminar, and the (molecular) viscosity plays a dominant role in momentum and heat or mass transfer. In the outer layer, called fully turbulent layer, turbulence plays major role. Finally, there is an interim region between the viscous sublayer and the fully turbulent layer where the effects of molecular viscosity and turbulence are equally important. Figure 9 illustrates these subdivisions of near-wall region, plotted in semi-log coordinates.

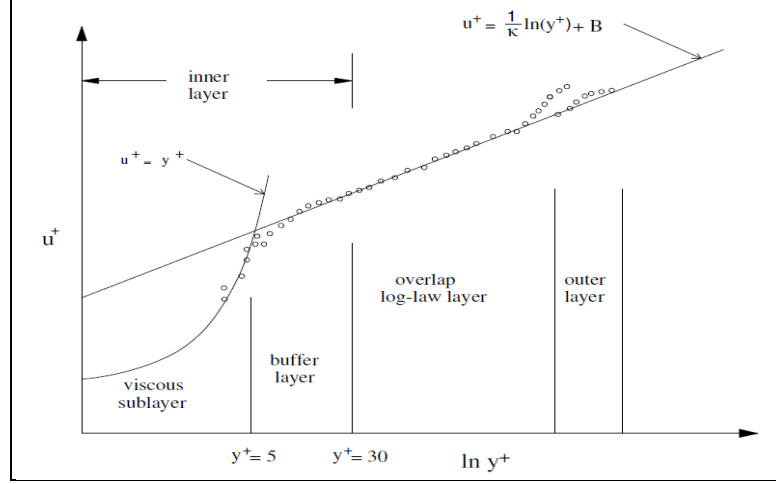


Figure 9. Subdivisions of near wall region

4.4.1 Inner layer

Here viscous (molecular) shear dominates and flow is almost laminar. The profile would depend on the wall shear stress τ_w , fluid properties (density ρ , and molecular viscosity μ) and distance y from the wall, but not upon the free stream parameters. Thus, the inner law –layer can be written as

$$\bar{u} = f(\tau_w, \rho, \mu, y) \quad [4.4.1]$$

Non-dimensional inner law-layer can be written as

$$\frac{\bar{u}}{v^*} = f\left(\frac{yv^*}{\nu}\right) \quad [4.4.2]$$

Where, ν is the kinematic viscosity, v^* is called as the wall friction velocity and is defined as:

$$v^* = \sqrt{\frac{\tau_w}{\rho}} \quad [4.4.3]$$

Figure 9 shows how the inner law-layer, rises from no slip at the wall to merge smoothly, at about $y^+ = 30$ to merge smoothly, with the overlap log-law

The inner layer can be further divided into two:

- Viscous Sublayer – at $y^+ \leq 5$, the velocity profile is linear. Here the turbulence is damped out and the boundary layer is dominated by viscous shear.
- Buffer Layer – when $5 \leq y^+ \leq 30$, the velocity profile is neither logarithmic (as in logarithmic overlap layer) nor linear as in viscous sublayer. It is a smooth merge between the two.

Turbulence modeling depends on how well the Inner layer is modeled. To model right up to the inner layer means high computational cost due to increase in mesh size. Modeling of the inner layer becomes extremely important, so that the tradeoff between cost and accuracy is achieved.

4.4.2 Outer layer

In the outer layer turbulent (eddy) shear dominates. The wall acts as a source of retardation of local velocity $\bar{u}(y)$ below the stream velocity U_0 . But this reduction of stream velocity is independent of kinematic viscosity μ but dependent on wall shear stress, layer thickness and freestream pressure gradient.

$$U_0 - \bar{u} = g\left(\tau_w, \rho, y, \delta, \frac{dp_0}{dx}\right) \quad [4.4.4]$$

Non-dimensional outer law-layer can be written as:

$$\frac{U_0 - \bar{u}}{v^*} = g\left(\frac{y}{\delta}, \xi\right) \quad [4.4.5]$$

Where, the local pressure gradient ξ and, δ is the boundary layer thickness.

$$\xi = \frac{\delta}{\tau_w} \frac{dp_0}{dx} \quad [4.4.6]$$

This is called velocity defect law, $(U_0 - \bar{u})$ is the defect or retardation of the flow due to wall effect.

4.4.3 Overlap Layer

Both types of shear i.e. molecular and eddy shear are equally important in this layer. The profile connects smoothly with the inner and outer layer.

$$\bar{u}_{inner} = \bar{u}_{outer} \quad [4.4.7]$$

Non dimensional profile can be written as,

$$\frac{\bar{u}}{v^*} = f\left(\frac{\delta v^*}{v} \frac{y}{\delta}\right) = \frac{U_0}{v^*} - g\left(\frac{y}{\delta}\right) \quad [4.4.8]$$

The function f contains a multiplicative constant and the function g an additive constant. It can only be true if both f and g are logarithmic functions. Thus for the overlap layer we have the following

Inner variables:

$$\frac{\bar{u}}{v^*} = \frac{1}{k} \ln \frac{yv^*}{v} + B \quad [4.4.9]$$

Outer variables:

$$\frac{U_0 - \bar{u}}{v^*} = -\frac{1}{k} \ln \frac{y}{\delta} + A \quad [4.4.10]$$

Where, κ and B are constants for flow past smooth impermeable walls. $k = 0.41$ and $B = 5.0$, A varies with pressure gradient ξ .

In the equation [4.4.9], the terms can be replaced by

$$u^+ = \frac{\bar{u}}{v^*} \quad [4.4.11]$$

$$y^+ = \frac{yv^*}{\nu} \quad [4.4.12]$$

Where, u^+ and y^+ are non dimensional velocity and length scales respectively.

4.5 Wall Functions vs. Near-Wall Modeling

The k - ϵ models, the RSM and the LES models are valid for fully turbulent flows i.e. flow in the regions far away from the walls. Therefore consideration has to be given to make these models suitable for wall-bounded flows.

Traditionally, there are two approaches for modeling the near-wall region.

- Wall function approach
- Near-wall model approach

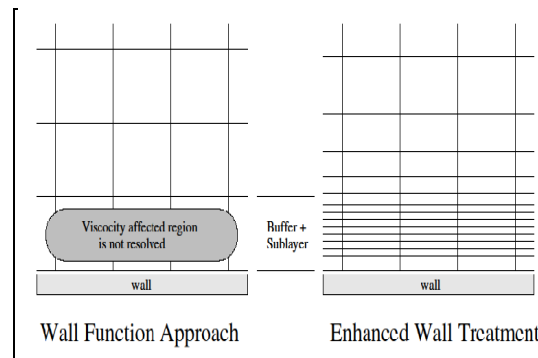


Figure 10. Wall function approach v/s Enhanced wall treatment

Wall Function Approach

The viscosity-affected inner region (viscous sublayer and the buffer layer) is not resolved. Instead, semi-empirical formulas called “wall functions” are used to bridge the viscosity-affected region between the wall and fully-turbulent region.

For high Reynolds number flows, wall function approach save computational resources and hence is economical. It is also quiet robust.

Near-wall Modeling Approach

The turbulence models can be modified to enable viscosity affected region to be resolved with mesh all the way to the wall. This is called Near Wall Modeling approach.

Wall functions approach cannot be used where low Reynolds number effects are prominent. In such cases wall function approaches ceases to be invalid, necessitating the need for near wall resolution of the mesh. The primary disadvantage of near wall approach is the high computational resource requirement.

4.6 Model Selection.

The $k-\varepsilon$ models, the RSM, and the LES model are primarily valid for turbulent core flows (i.e., the flow in the regions somewhat far from walls). Consideration therefore needs to be given as to how to make these models suitable for wall-bounded flows. The Spalart-Allmaras and $k-\omega$ models were designed to be applied throughout the boundary layer, provided that the near-wall mesh resolution is sufficient.

In this simulation study, the $k-\varepsilon$ turbulent model with Standard wall function was used. The reason of such selection is the near wall mesh resolution of the generated grid.

The $k-\varepsilon$ turbulent model is one of the most common models. It is a two equation model that includes two extra transport equations to represent the turbulent properties of the fluid flows. However, the $k-\omega$ SST model was also employed in the simulations, which did not produced realistic results and therefore did not fit well with current model. Issues with $k-\omega$ SST model are explained in the next section.

4.6.1 Issues with $k-\omega$ SST model

Many researchers use $k-\omega$ SST or Spalart-Almaras turbulence models for prediction of the power coefficient of wind turbines with structured type of mesh in computational domain by having very fine resolution near the blades and the hub region. Contrary to expectations, the $k-\omega$ SST model performed poorly in this study. Work by Bardina, [44] provides a possible explanation. The authors have shown that two-equation turbulence models are very sensitive to the grid arrangement on the normal direction. According to Bardina, $k-\omega$ SST predicts about 5% deviation of skin friction at y^+ being as small as 1.5 and the trend to predict worse result as y^+ increase. The current grid use y^+ in the range between 30 and 300, which is not sufficient for $k-\omega$ SST. Other researchers e.g. Sorensen [14] and Duque [12] used y^+ around 1, and have reported good results.

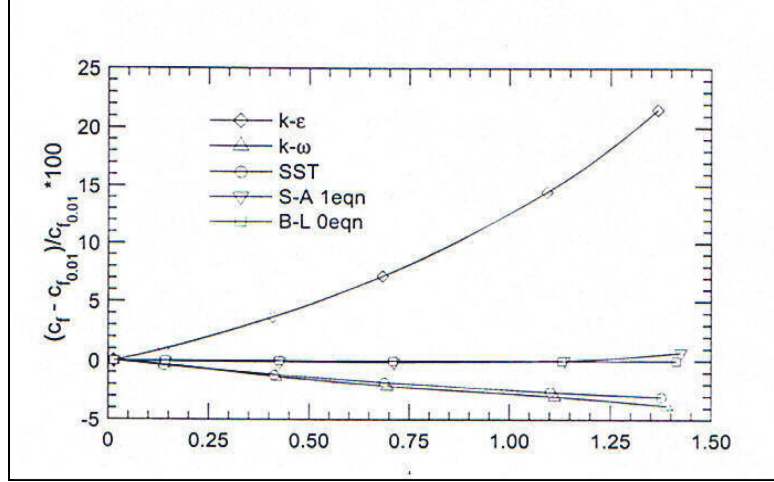


Figure 11. Sensitivity to the distance of the first point to the wall, (y^+)

Figure 11 also shows the SA model is less sensitive to the size of y^+ , possibly due to the inherent damping provided by the damping function. In contrast, the $k-\omega$ SST does not have a wall damping function. Furthermore, the process $k-\omega$ SST uses to transition from $k-\omega$ to $k-\epsilon$ might require a very fine grid in the normal direction in order to make a smooth transition [11].

The grid used in this study is therefore inadequate for this turbulence model. . By resolving the mesh right up to the viscous sublayer, the number of elements is increased multifold forcing the aspect ratio, near the wall region, also to increase.

Computer hardware used (2GB RAM, dual core processor) in the simulations was not capable to handle such high number of grids and capacity of memory was not sufficient.

4.6.2 $k-\epsilon$ Turbulent Model

The standard $k-\epsilon$ model is a semi-empirical model [33] based on model transport equations for the turbulence kinetic energy k and its dissipation rate ϵ . The model

transport equation for k is derived from the exact equation, while the model transport equation for ε was obtained using physical reasoning and bears little resemblance to its mathematically exact counterpart. In the derivation of the k - ε model, it was assumed that the flow is fully turbulent, and the effects of molecular viscosity are negligible. The standard k - ε is therefore valid only for fully turbulent flows.

The turbulence kinetic energy, k and its rate of dissipation, ε are obtained from the following transport equations:

$$\frac{d}{dt}(\rho k) + \frac{d}{dx_i}(\rho k u_i) = \frac{d}{dx_j} \left[\left(\mu + \frac{\mu_t}{\sigma_k} \right) \frac{dk}{dx_j} \right] + G_k + G_b - \rho \varepsilon - Y_M + S_K \quad [4.6.1]$$

$$\frac{d}{dt}(\rho \varepsilon) + \frac{d}{dx_i}(\rho \varepsilon u_i) = \frac{d}{dx_j} \left[\left(\mu + \frac{\mu_t}{\sigma_\varepsilon} \right) \frac{d\varepsilon}{dx_j} \right] + C_{1\varepsilon} \frac{\varepsilon}{k} (G_k + C_{3\varepsilon} G_b) - C_{2\varepsilon} \rho \frac{\varepsilon^2}{k} + S_\varepsilon \quad [4.6.2]$$

Where,

G_k - Turbulence kinetic energy due to mean velocity gradients

G_b - Turbulence kinetic energy due to buoyancy

Y_M - Contribution of fluctuating dilation in compressible turbulence to overall dissipation rate

$C_{1\varepsilon}, C_{2\varepsilon}, C_{3\varepsilon}$ - Experimentally determined constants

$\sigma_\varepsilon, \sigma_k$ - Experimentally determined turbulent Prandtl numbers for k and ε

S_K, S_ε - Source terms

The turbulent viscosity is computed as

$$\mu_t = \rho C_\mu \frac{k^2}{\varepsilon} \quad [4.6.3]$$

Where, C_μ is a constant.

4.7 Modeling Flows with Rotating Reference Frames

The equation of fluid flow is usually solved by Fluent in stationary (or inertial) reference frames. However, there are many problems that require the equations be solved in a moving (or non-inertial) allows to model problems involving reference frame. Rotating rotor of wind turbine is such case. This kind of modeling capabilities allows to model problems involving moving parts by activating moving reference frames in selected cell zones. When this option is activated, the equations of motion are modified to incorporate the additional Coriolis acceleration terms which occur due to the transformation from the stationary to the moving reference frame. By solving these equations in a steady-state manner, the flow around the moving parts can be modeled. Moving reference frames (MRF) was used in current simulations, which is briefly highlighted in the next section

4.7.1 Relative Velocity Formulation and MRF

Consider a coordinate system which is rotating steadily with angular velocity $\vec{\omega}$ relative to a stationary (inertial) reference frame. The origin of the rotating system is located by a position vector \vec{r}_o (see Figure 12)

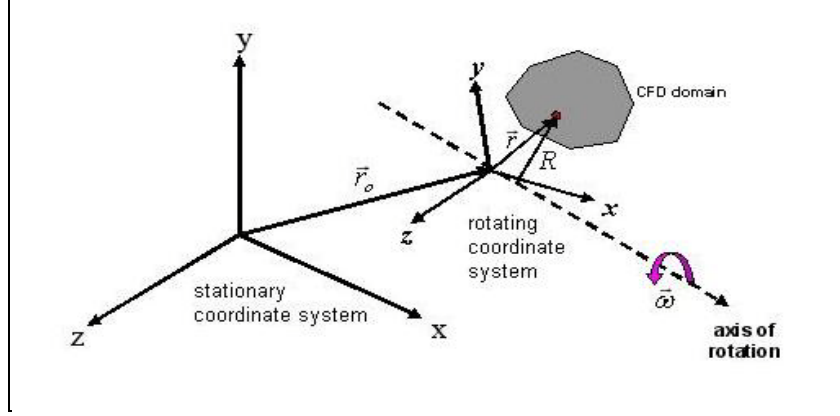


Figure 12. Coordinate system for moving reference frame

The fluid velocities can be transformed from the stationary frame to the rotating frame using the following relations:

$$\vec{v}_r = \vec{v} - \vec{u}_r \quad [4.7.1]$$

And,

$$\vec{u}_r = \vec{\omega} \times \vec{r} \quad [4.7.2]$$

Where \vec{v}_r is the relative velocity (the velocity viewed from the rotating frame), \vec{v} is the absolute velocity (the velocity viewed from the stationary frame), and \vec{u}_r is the whirl velocity (the velocity due to the moving frame).

For the relative velocity formulation, the governing equations of fluid flow for a steadily rotating frame can be written as follows:

Conservation of mass:

$$\frac{\partial \rho}{\partial t} + \nabla \cdot (\rho \vec{v}_r) = 0 \quad [4.7.3]$$

Conservation of momentum:

$$\frac{\partial}{\partial t}(\rho \vec{v}_r) + \nabla \cdot (\rho \vec{v}_r \vec{v}_r) + \rho(2\vec{\omega} \times \vec{v}_r + \vec{\omega} \times \vec{\omega} \times \vec{r}) = -\nabla p + \nabla \cdot (\overline{\overline{\tau}}_r) + \vec{F} \quad [4.7.4]$$

The momentum equation contains two additional acceleration terms: the Coriolis acceleration ($2\vec{\omega} \times \vec{v}_r$) and the centripetal acceleration ($\vec{\omega} \times \vec{\omega} \times \vec{r}$).

4.8 Boundary Conditions (BC)

Once 3-D model for the wind turbine rotor and computational domain is created, the flow boundary conditions have to be specified. For obtaining accurate simulation results, it is a very critical that these boundary conditions are specified properly. The following boundary conditions were used in the model:

Wall (no-slip)

Wall boundary conditions (BC) are used to bound fluid and solid region. In our case would be blade surface and the atmospheric air.

Velocity-inlet

BC is used to specify the defined air flow velocity, along with all relevant scalar properties of the flow, like turbulent model at flow inlets. The total pressure is not fixed but will rise to whatever value is necessary to give the necessary velocity distribution. In Fluent this boundary condition is intended for incompressible flows and it has to be kept as far away from a solid obstruction as possible.

When a velocity inlet boundary condition is defined, Fluent computes the mass flow rate, \dot{m} as

$$\dot{m} = \int \rho \vec{v} \cdot d\vec{A} \quad [4.8.1]$$

Outflow

Outflow boundary conditions are used to model flow exits where the details of the flow velocity and pressure are not known prior to solving the flow problem. This boundary condition is appropriate where the exit flow is close to fully developed condition. It assumes that there is a zero streamwise pressure gradient for all flow variables except pressure.

Symmetry

Symmetry boundary condition is used when the physical geometry of interest, and the expected pattern of the flow/thermal solution, has mirror symmetry. It can also be used to model zero-shear slip walls in viscous flows. In such cases the domain extends are kept at a distance as far as possible from the wall (turbine), so that there is little effect of boundary on the flow.

The properties of symmetry boundary conditions are as follows

- Zero flux of all quantities across a symmetry boundary.
- There is no convective flux across a symmetry plane: the normal velocity component at the symmetry plane is thus zero.

Periodic

Periodic boundary conditions are used when the physical geometry of interest and the expected pattern of the flow/thermal solution have a periodically repeating nature. By

using a periodic boundary the number of grids can be reduced enabling finer grids. Given below Figure 13 depicts the boundary conditions in 2-D. The first figure shows the blade in full and the second one with $1/3^{\text{rd}}$ of the turbine and the third figure shows the velocity-inlet and outflow boundaries.

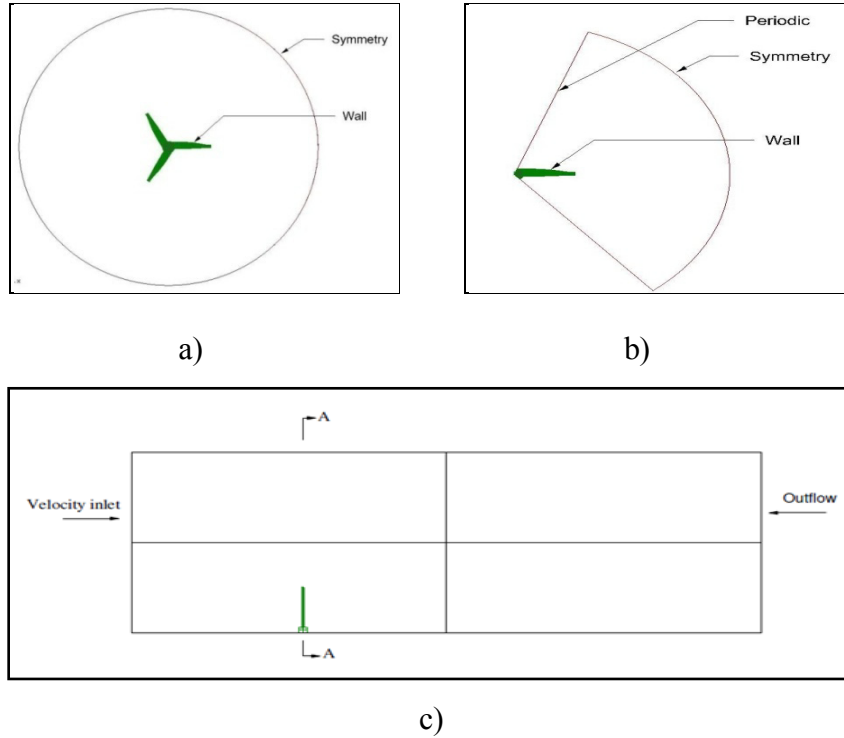


Figure 13. a) 2-D views of the turbine and the applied boundary conditions with cylindrical domain, b) periodic view, c) velocity inlet and outflow

4.9 Modeled Blade

The foil series which was used for the blade design was the NACA 638xx [34]. The first digit in the series when multiplied by $3/2$ yields the design lift coefficient C_l in tenths (0.9%). The second digit when divided by 2, defines the maximum camber (in tenths) location. In our case, it is located at 19% of the chord length, measured from leading

edge. Camber allows a foil to generate lift at an angle of attack α of zero degree. The last two digits in the series represent the thickness to the cord length (t/c) ratio. A blade radius of 3 meters and hub radius of 375 mm was considered. The following table shows the particulars of the turbine blade and the hub.

Main Particulars	
Rotor radius	3m
Blade length	2.625m
Hub radius	0.375m
Number of blades	3
Pitch	15 degree
Foil Type	NACA 638xx

Table 1. Turbine's particulars

r/R	Radius r(mm)	c/R	Pitch Distribution(deg)	t/c (%)
0.2	600	0.125	15	24
0.25	750	0.1203	12.1	22.5
0.3	900	0.1156	9.5	20.7
0.35	1050	0.1109	7.6	19.5
0.4	1200	0.1063	6.1	18.7
0.45	1350	0.1016	4.9	18.1
0.5	1500	0.0969	3.9	17.6
0.55	1650	0.0922	3.1	17.1
0.6	1800	0.0875	2.4	16.6
0.65	1950	0.0828	1.9	16.1
0.7	2100	0.0781	1.5	15.6
0.75	2250	0.0734	1.2	15.1
0.8	2400	0.0688	0.9	14.6
0.85	2550	0.0641	0.6	14.1
0.9	2700	0.0594	0.4	13.6
0.95	2850	0.0547	0.2	13.1
1	3000	0.05	0	12.6

Table 2. Foil Section Characteristics

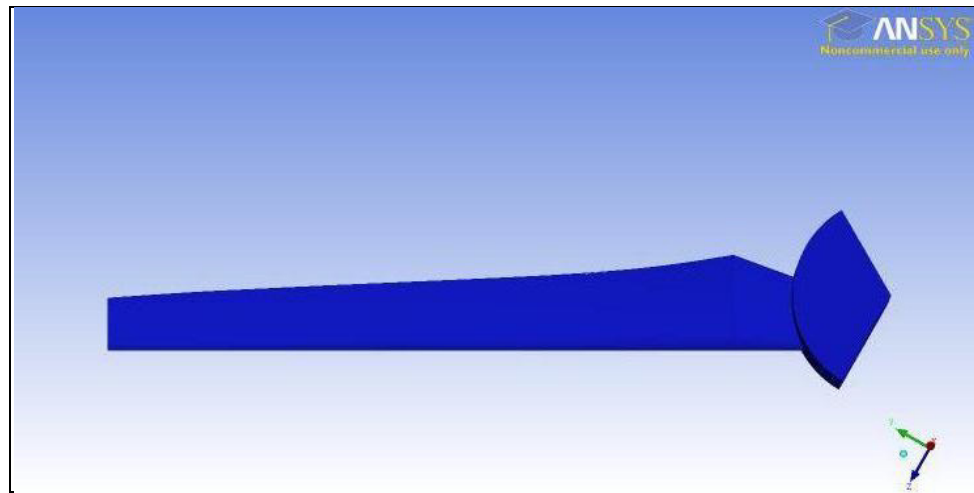


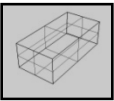
Figure 14. Modeled blade (RhinoCeros 4.0).

CHAPTER

5. MESH GENERATION

Grid generation is often considered as the most time consuming part of CFD simulation [35]. The quality of the grid plays a direct role on the quality of the analysis, regardless of the flow solver used. Mesh can be classified as structured, unstructured and hybrid types.

5.1 Structured Grid Methods

Here mesh grid is laid out in a regular repeating pattern called a block. These types of grids utilize quadrilateral elements in 2D and hexahedral  elements in 3D in a computationally rectangular array. Really good structured grid generators utilize sophisticated elliptic equations to automatically optimize the shape of the mesh for orthogonality and uniformity.

Advantages of structured grids

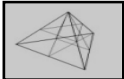
- Allows the user a high degree of control
- Hexahedral and quadrilateral elements are very efficient at filling space, support a high amount of skewness and stretching before the solution will be significantly affected.

- Grid is most often flow-aligned, thereby yielding greater accuracy within the solver.
- They typically require the lowest amount of memory for a given mesh size and execute faster because they are optimized for the structured layout of the grid.
- Easier post-processing because the logical mesh planes make excellent reference points for examining the flow field and plotting results.

Disadvantages of structured grids

- Requires higher expertise to lay out an optimal block structure for an entire model
- Time consuming process.

5.2 Unstructured Grid Methods

Unstructured grid methods utilize an arbitrary collection of elements to fill the domain. Because the arrangement of elements has no discernible pattern, the mesh is called unstructured. These types of grids typically utilize triangles in 2D and  tetrahedral in 3D. As with structured grids, the elements can be stretched and twisted to fit the domain. The automatic meshing algorithm typically involves meshing the boundary or adding points in the interior and reconnecting the elements.

Advantages of unstructured grids

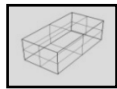
- Very little user input required
- Enables the solution of a very large detailed problems in a relatively short period of time

Disadvantages of unstructured grids

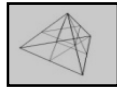
- Lack of control when laying out the mesh
- Problem with stretching triangle or tetrahedral elements. Grid is limited to being largely isotropic, i.e. all the elements have roughly the same size and shape
- Reliance on good CAD data. Errors in CAD model will yield the failure.
- Solvers require more memory and have longer execution times

5.3 Hybrid Grid Methods

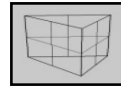
Hybrid grid methods are designed to take advantage of the positive aspects of both volumes structured and unstructured grids. Hybrid grids can contain hexahedral,



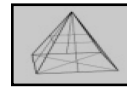
tetrahedral



prismatic



and



pyramid

elements in 3D and triangles and quadrilaterals in 2D. Hexahedral elements are excellent near solid boundaries (where flow field gradients are high) and afford the users a high degree of control. Prismatic elements (usually triangles extruded into wedges) are useful near wall gradients. In most all cases, tetrahedral elements are used to fill the remaining

Advantages of Hybrid Grids

- Both structured and unstructured meshes can be used simultaneously
- Control of the shape and mesh distribution

Disadvantages of Hybrid Grids

- Requires higher expertise
- Are less robust than unstructured methods

5.4 Mesh Quality

The quality of the mesh plays a crucial role in the accuracy and stability of the numerical computation. The attributes associated with mesh quality are node point distribution, smoothness, and skewness.

Node Density and Clustering

Solution for flows such as: shear layers, separated regions, shock waves, and boundary layers and mixing zones, depends on the density and distribution of nodes in the mesh. In many cases, poor resolution in critical regions can dramatically alter the flow characteristics. For example, the prediction of separation due to an adverse pressure gradient depends heavily on the resolution of the boundary layer upstream of the point of separation. Proper resolution of the mesh for turbulent flows is also very important: due to the strong interaction of the mean flow and turbulence, the numerical results for turbulent flows tend to be more susceptible to grid dependency than those for laminar flows.

Depending on the cell types in the mesh, different quality criteria are evaluated [31].

- Cell squish on all meshes.
- Cell equivolume skew on tri/tet elements
- Face squish on polyhedral meshes
- Aspect ratio on all meshes

Cell squish

It is a measure of deviation in orthogonality with respect to cell faces. It is calculated from the dot product of each vector pointing from the centroid of a cell towards the center of each of its faces, and the corresponding face area vector.

$$\max \left[1 - \frac{\vec{A}_i \cdot \vec{r}_{co / xfi}}{|\vec{A}_i| |\vec{r}_{co / xfi}|} \right] \quad [5.4.1]$$

Where, \vec{A}_i is the surface area vector and $\vec{r}_{co / xfi}$ is the distance between centroid of a cell to its face center. Cell squish of 1 means worst quality cell.

Cell equivolume skew on tri/tet elements

It is non-dimensional parameter calculated using the volume deviation method, and is defined as:

$$\frac{\text{optimal cell size} - \text{cell size}}{\text{optimal cel size}} \quad [5.4.2]$$

Where, optimal cell size is the size of an equilateral cell with the same circumradius. A value of 0 indicates a best case equilateral cell and value of 1 indicates a completely degenerate cell.

Face squish on polyhedral meshes

It is a measure of the quality of a mesh, and is calculated from the dot products of each face area vector, and the vector that connects the centroids of a two adjacent cells as

$$1 - \frac{\vec{A}_i \cdot \vec{r}_{co/xfi}}{|\vec{A}_i| |\vec{r}_{co/xfi}|} \quad [5.4.3]$$

Where, \vec{A}_i is the surface area vector and $\vec{r}_{co/xfi}$ is the distance between centroids. Face squish of 1 means worst quality cell.

Aspect ratio on all meshes

Figure 15 shows the parameters that are used to evaluate the aspect ratio. This ratio is a measure of the stretching of a cell. It is computed as the ratio of a maximum value to the minimum value of the following distances: the distance between the cell centroid and face centroids, and the distances between the cell centroid and nodes. For a unit cube, the maximum distance is 0.866, and the maximum distance is 0.5, so the aspect ratio is 1.732. This type of definition can be applied to any type of mesh, including polyhedral.

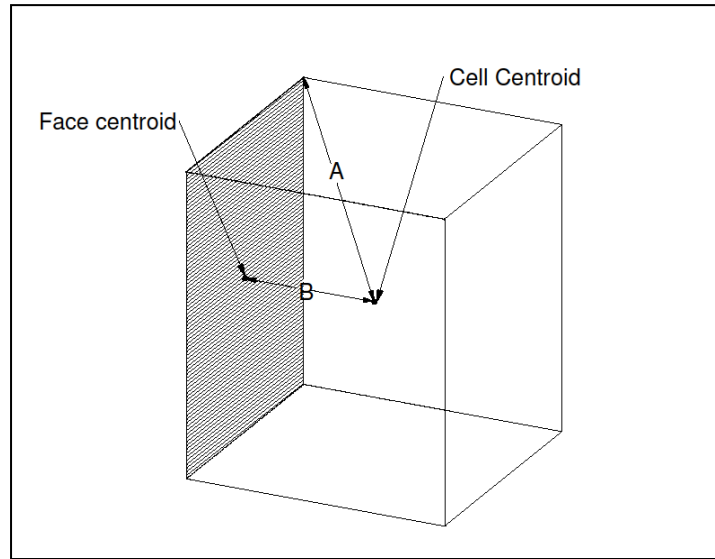


Figure 15. Aspect ratio=A/B

5.5 Computational Grid and Domain

Model is including neither the tower nor ground and a uniform wind speed profile was assumed at the entrance of the domain. The pre-processor ANSYS ICEM CFD 12.0 was used to build a tetrahedral mesh of approximately 1.14 million volume elements. Periodic section of the hub and the blade was modeled for CFD analysis. By applying periodicity, high number of mesh elements was put in 1/3 section of the computational domain. As it was explained earlier, the higher the number of elements, the better is the accuracy. Later, results will be replicated into other two sections. Tetrahedral and prismatic elements were created on the blade and hub surface, which are also very effective at filling space of entire domain, supporting a high amount of skewness and stretching.

Figure 16 shows the mesh in the cylindrical domain bonded around the blade and periodic surfaces.

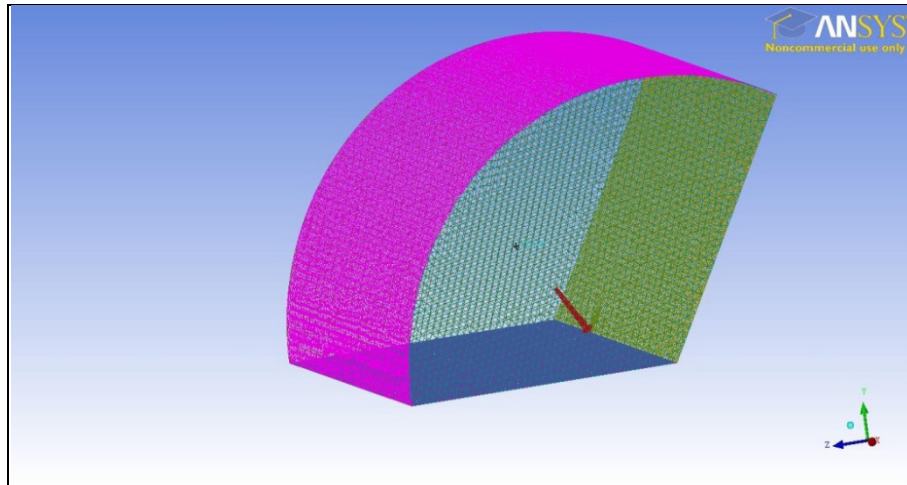


Figure 16. Graphical visualization of computational domain (periodic)

Figure 17 shows the dimensions of the domain extends in axial and radial directions. Computational domain was cylindrical shape extending in axial direction roughly two diameters upstream and five diameters downstream of the rotor. In the vertical plane of the rotor, the domain diameter was 1.5 times of the rotor diameter at the inlet and the outlet.

These dimensions were considered in order to accommodate the available computing resources, since all simulations must be run on regular personal computer.

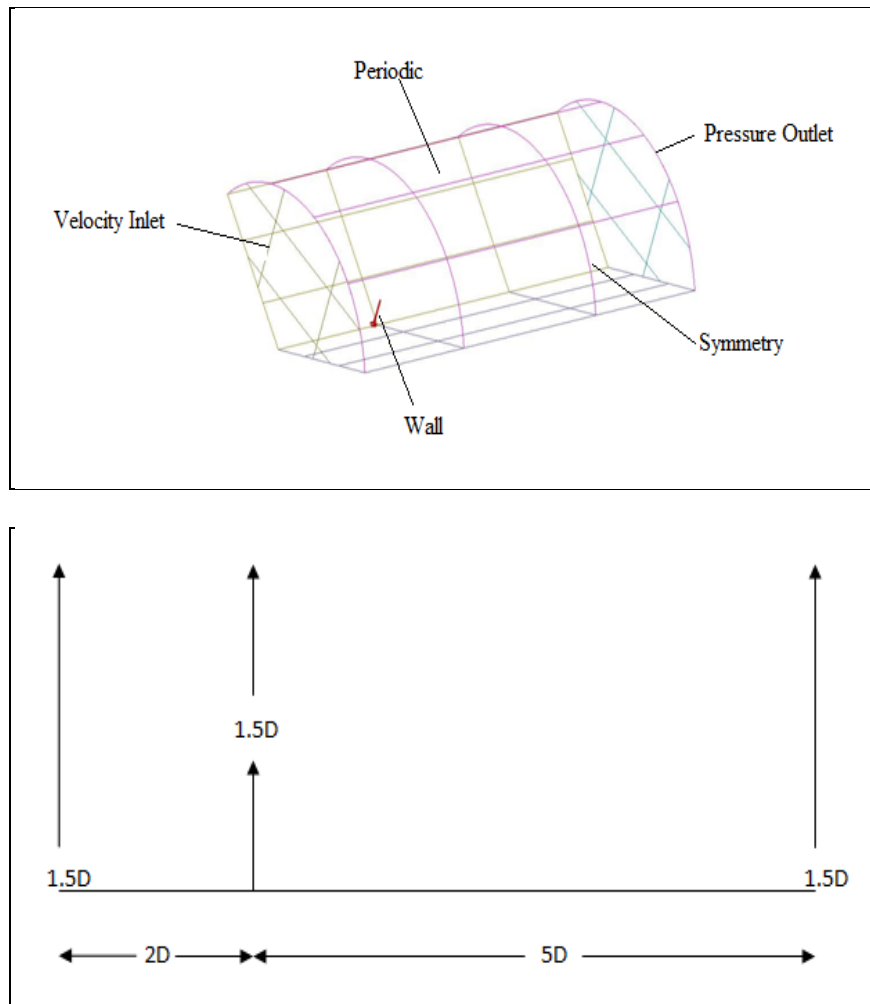


Figure 17. Computational Domain Dimensions

In Figure 17 also shown the boundary conditions imposed: at the inlet face and the lateral boundary undisturbed uniform wind velocity and turbulence were fixed; static pressure was set at the outlet; no-slip condition was selected for the blade and the hub surfaces. Figure 18 shows the near wall mesh around the hub and blade section. Two-dimensional cut plane at the blade in Figure 20 is showing the tetrahedral elements at the plane of the rotor. Figures 19 and 21 are illustrating the mesh on the blade along with periodic hub section and near wall resolution of y^+ , respectively.

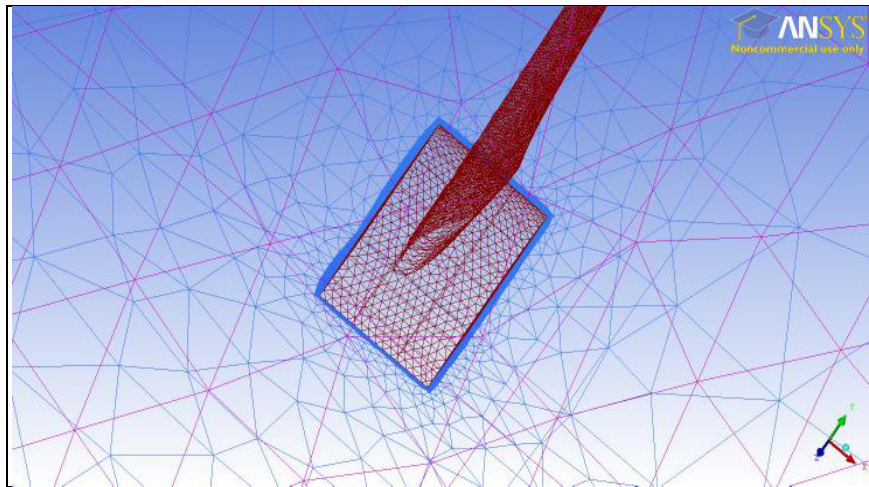


Figure 18. Blade and the hub embedded in tetra mesh

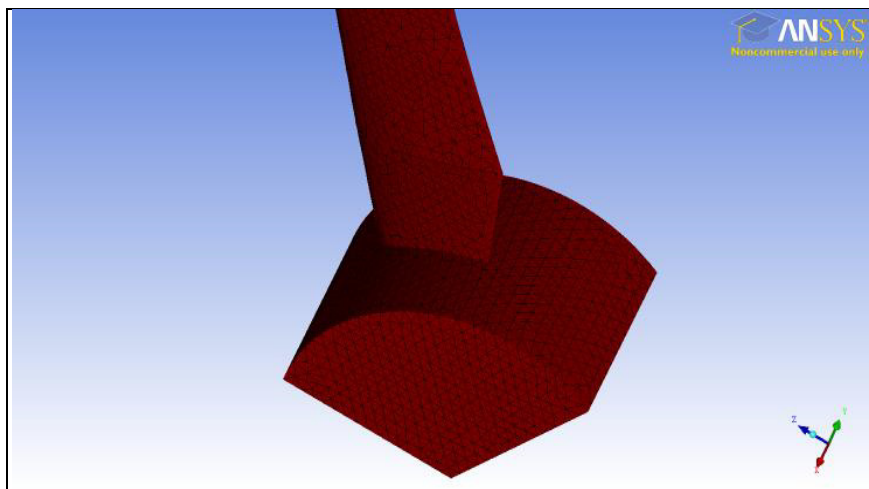


Figure 19. Mesh of the root of blade and hub section

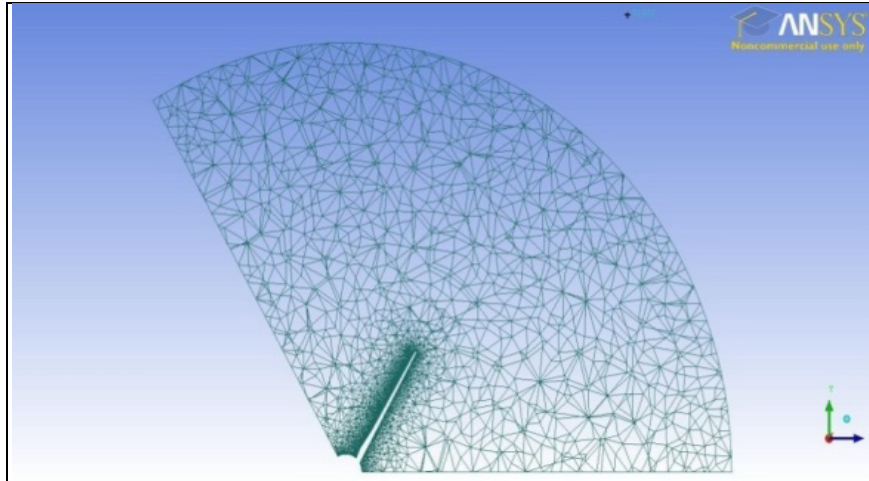


Figure 20. Mesh cut plane at blade

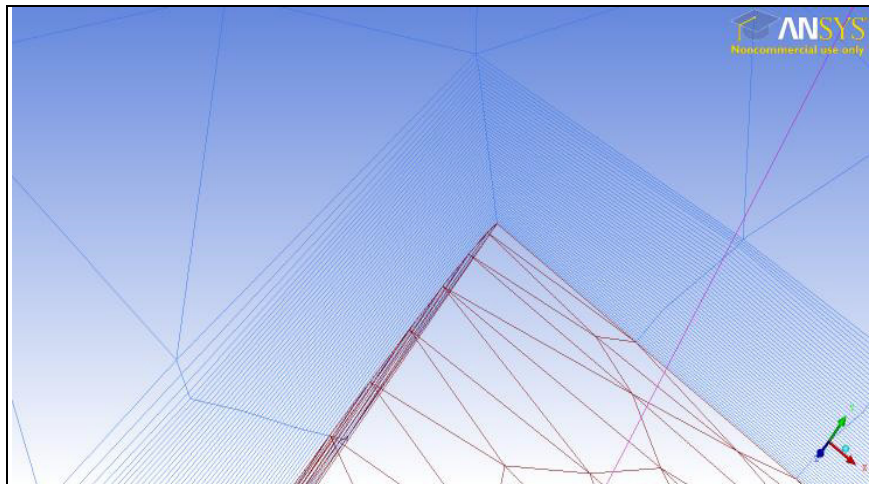


Figure 21. y^+ resolutions at prism layers

CHAPTER

6. VALIDATION OF CFD MODEL RESULTS

6.1 NREL Phase VI Experiment

The US Department of Energy's (DOE) National Renewable Energy Laboratory (NREL) tested a 10-meter diameter research wind turbine in the world's largest wind tunnel. The test was undertaken in NASA's 24.4 by 36.6 meters (80' by 120') wind tunnel. The tunnel is primarily used for determining low and medium-speed aerodynamic characteristics of full-scale aircrafts and rotorcrafts. The tunnel is powered by six 18,000 hp fans that produce test section wind velocities up to 50 m/s (115 mph). The NREL/NASA Phase VI test turbine was built from a Grumman Wind Stream-33. A 10 m diameter, stall-regulated turbine with full-span pitch control and had a power rating of nearly 20 kW. Many modifications were made to this turbine, prior to the wind tunnel test. The phase VI rotor designed by Giguère and Selig [9] under contract by NREL from March 1998 through March 1999. The turbine used during the wind tunnel test was a two-bladed turbine, with twisted and tapered blades, and was tested in both upwind and downwind rotor configurations. Further information about wind tunnel data can be found in the document by Hand [35]. In this blind run, the RANS simulations by Sorensen [36] correlated best with measurements. With the same methodology, Madsen [37] studied

the effects of yaw on air loads. The performance predictions by Xu [38] were also in very good agreement with the experiment, particularly at high wind speeds.



Figure 22. Wind Turbine Testing in NASA (10 m in diameter)
www.wind-nrel.gov/amestest



Figure 23. NASA-Ames 80' x 120' Wind Tunnel

The NREL turbine has been simulated under a free stream wind speed ranging from 4 to 12 m/s, with low inflow turbulence levels (10% and length scale of 1 m). The Phase VI

rotor is the first in which a linear taper was specified so that the chord length at 80% span was 457 mm and 305 mm at the tip. It is exclusively made of S809 airfoil sections from root to tip. Figure 24 shows the blade characteristics and shape.

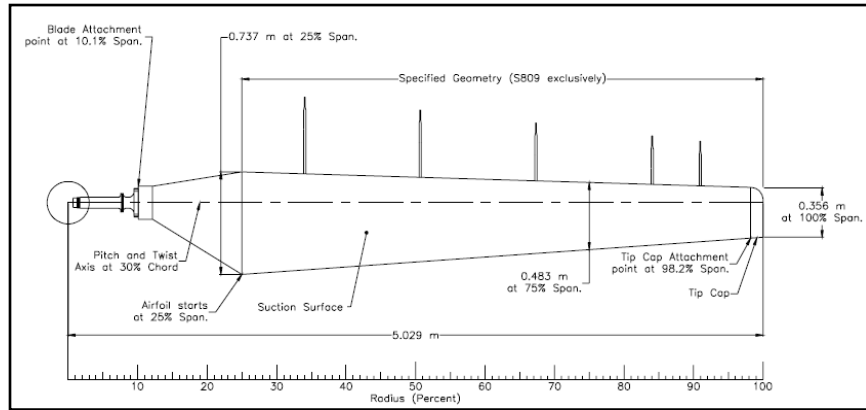


Figure 24. NREL Phase VI rotor blade

6.2 CFD vs. Experiment

The commercial code Fluent was used to validate results with NREL Unsteady Aerodynamics Experiment (UAE) Phase VI turbine: The performance of a wind turbine can be characterized by three main indicators power, torque and thrust and letting the vary wind speed [19]. The power determines the amount of energy extracted by the rotor. The torque determines the size of the gear box. Finally, the thrust has a great influence on the structural design of the tower. Recalling the objectives of the thesis, turbine's power in terms of efficiency C_p and also the torque were considered in validation. Simulations were performed by using the $\kappa - \varepsilon$ turbulent model with Standard wall function.

COUPLED explicit solution algorithm was employed with Second Order Upwind discretization scheme for kinetic energy k and its dissipation rate ε . Tolerance value has been set at 10^{-6} for convergence criteria. Also, moving reference frame was selected with angular velocity of $\omega = -23.33$ rad/s (TSR=7). Negative sign indicates that tangential velocity acts in the opposite direction to that of the rotation. Inflow velocity was kept constant at 10 m/s and TSR was varied by increasing rotational speed.

It is convenient to express the performance by means of non-dimensional, characteristic performance (power, torque and thrust coefficients) as a function of tip speed ratio.

6.2.1 Calculation of Efficiency C_p

There are two methods available for calculating the power coefficient C_p of the rotor: one can obtain the torque (moment, N-m) values from CFD results and multiply it by angular velocity ω . Results will yield the power of the turbine.

$$P = T\omega \quad [6.2.1]$$

By applying equation [2.1.4] presented in Chapter 2, power coefficient C_p can be determined.

Other method for obtaining the efficiency C_p of the turbines is the implementation of the Actuator Disk Theory. Free stream velocity V_0 and downstream velocity V_3 are obtained from CFD and the equations [2.1.2] to [2.1.5] will again result the power coefficient. An overview of Actuator Disk Theory can be found in Appendix A. In current study, this concept was preferred for calculations of turbine's power coefficients at different TSRs.

Method is highly suitable and convenient, especially when computational grid resolution is not very fine near the blades and the hub and torque values are not very reliable.

Figure 25 shows relationship of two turbines power coefficients plotted against non-dimensional tip speed ratios. Maximum C_p of CFD results is registered at 40%, producing approximately 7KW of mechanical shaft power. This corresponds to TSR 7. UAE turbine achieves a pick efficiency of approximately 36% at tip speed ratio of approximately 5.5 in controlled wind tunnel environment. Wind speed for experimental turbine was measured 6.9 m/s and rotors rotational speed is 72 rpm. Considering variations in rotors diameters and entering flow velocities, calculated error of 10 % is within the acceptance. Simulated power curve has a similar trend like other typical turbines.

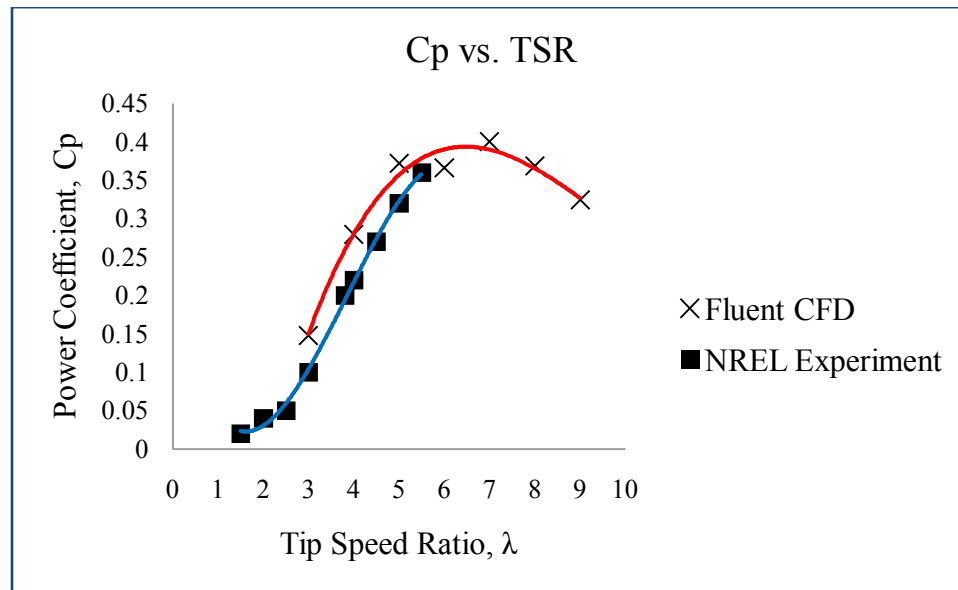


Figure 25. C_p versus λ comparison plot CFD vs. experiment

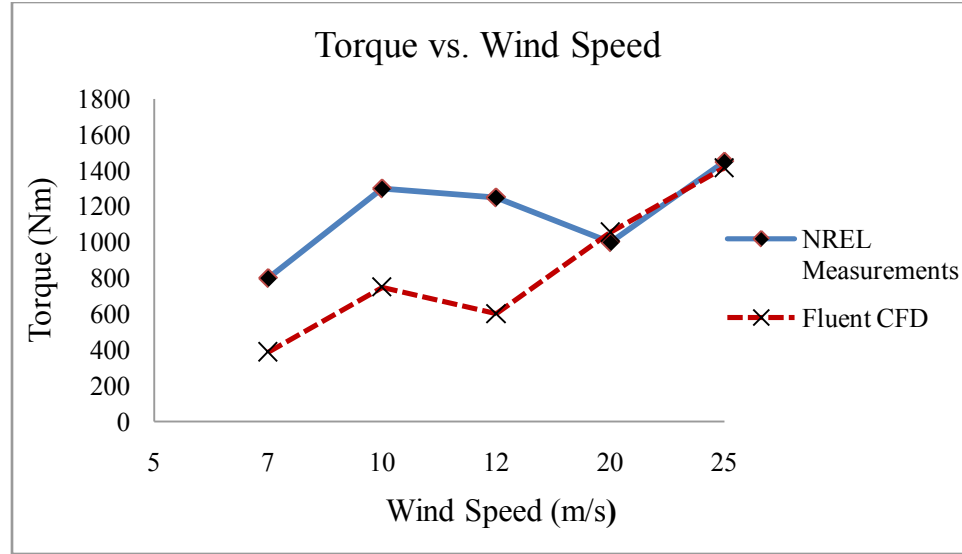


Figure 26. Torque vs. wind speed

Figure 26 shows the torque versus wind speed relationship for NREL rotor and modeled CFD turbine. The measurements were done at various wind speeds that can be classified as: low wind speed (7m/s), intermediate wind speed (10 m/s, 12 m/s) and high wind speed (20m/s and 25m /s) regimes. For low speeds the performance of modeled turbine is under predicted, however, the power output increases with wind speed. In intermediate wind speed regime, flow starts separate over the blade to maintain the power output around the rated power of the generator. In high wind speed regime power increases and it is closely agrees with experimental values. Other authors like S. Benjanirat [11], Duque [12] and Sørensen [14] used Spalart Allmaras DES and $k-\omega$ SST turbulence models and have reported better results.

CHAPTER

7. RESULTS AND DISCUSSIONS

7.1 Flow Visualization

This chapter deals with the flows before and after the blade, its surrounding area and the wake of the turbine. A comparison of axial velocity distribution for various TSR's is presented. A case TSR 7 is taken for studying the flow characteristics. The inlet stream velocity is fixed at 10 m/s and the blade has a rotational speed of $\omega = -23.33$ rad/s. The moving reference frame was modeled with a fluid rotating around the blade. Turbine itself presented as moving wall with rotational speed of 0 rad/s with respect to rotating fluid (air in this case). The axial, radial and tangential velocity contours are plotted in different sections along the x-axis (flow direction). Normalized axial velocity was also plotted at different points along the x-axis. Flow is also visualized in $y=0$ plane along with pressure distribution plots along the flow direction. Rotational vortices effects along with Eddy viscosity contours are also shown. Figure 27(a) and 27(b) illustrates axial velocity contours at different x/D locations. The contours are plotted by taking clipped surface from the center of the hub to a radially outward distance of 4 m. This allows visualizing the contours close to near-blade region. Velocity reduces as the flow approaches the rotor. According to actuator disk theory axial velocity is reduced at the

rotor plane (due to induction factor) in the presence of the rotor and it is confirmed in $x/D=0$ contour. The flow past the turbine includes some zero and negative axial velocities. This can be explained by presence of the blunt (modeled for simplicity) hub surface which disturbs the smooth aerodynamic transition of the flow wakes and also the presence of some mixing flows and other backflow effects.

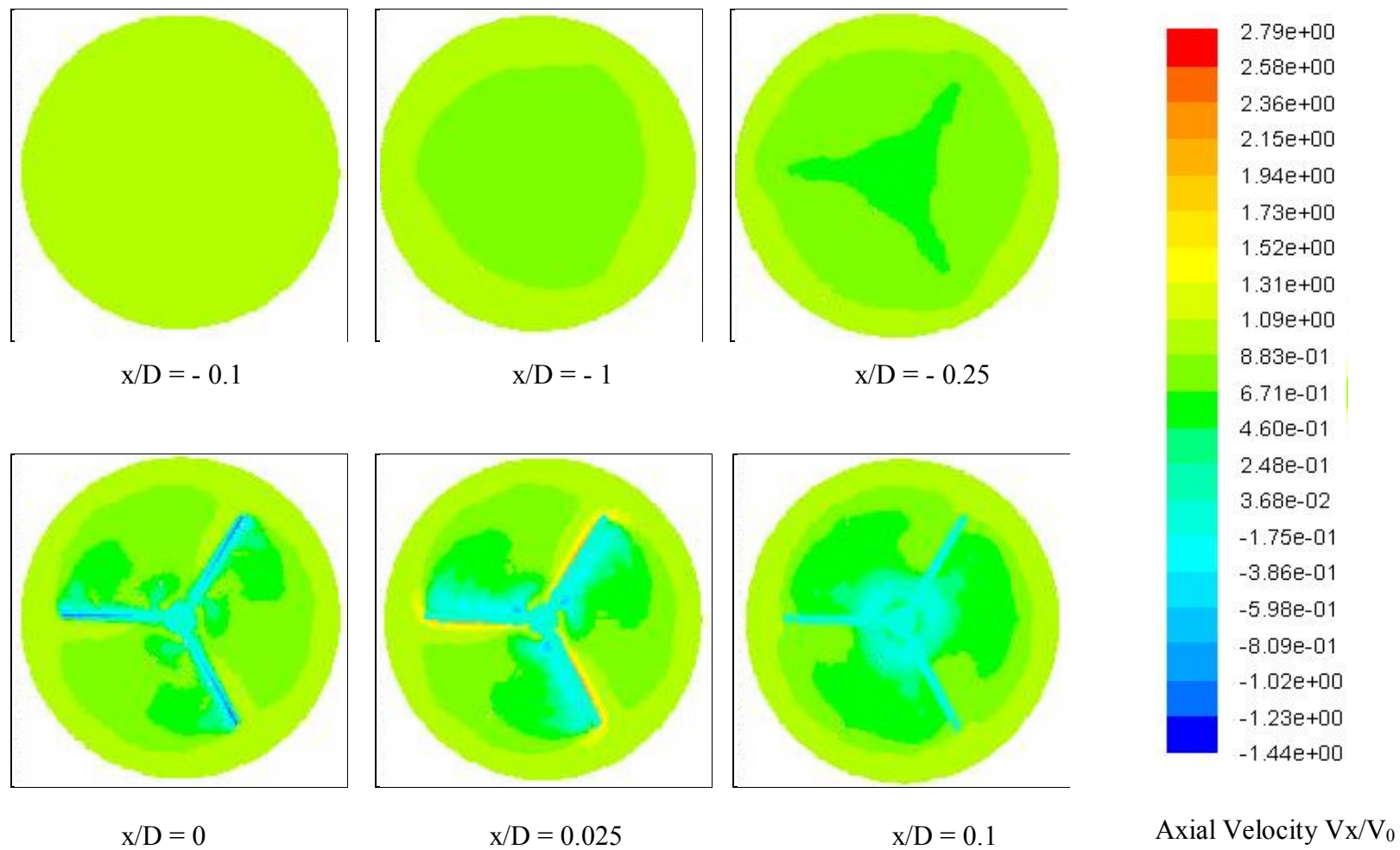


Figure 27. (a) Axial velocity contours at different x/D locations for $TSR=7$ with stream velocity $V_0=10$ m/s

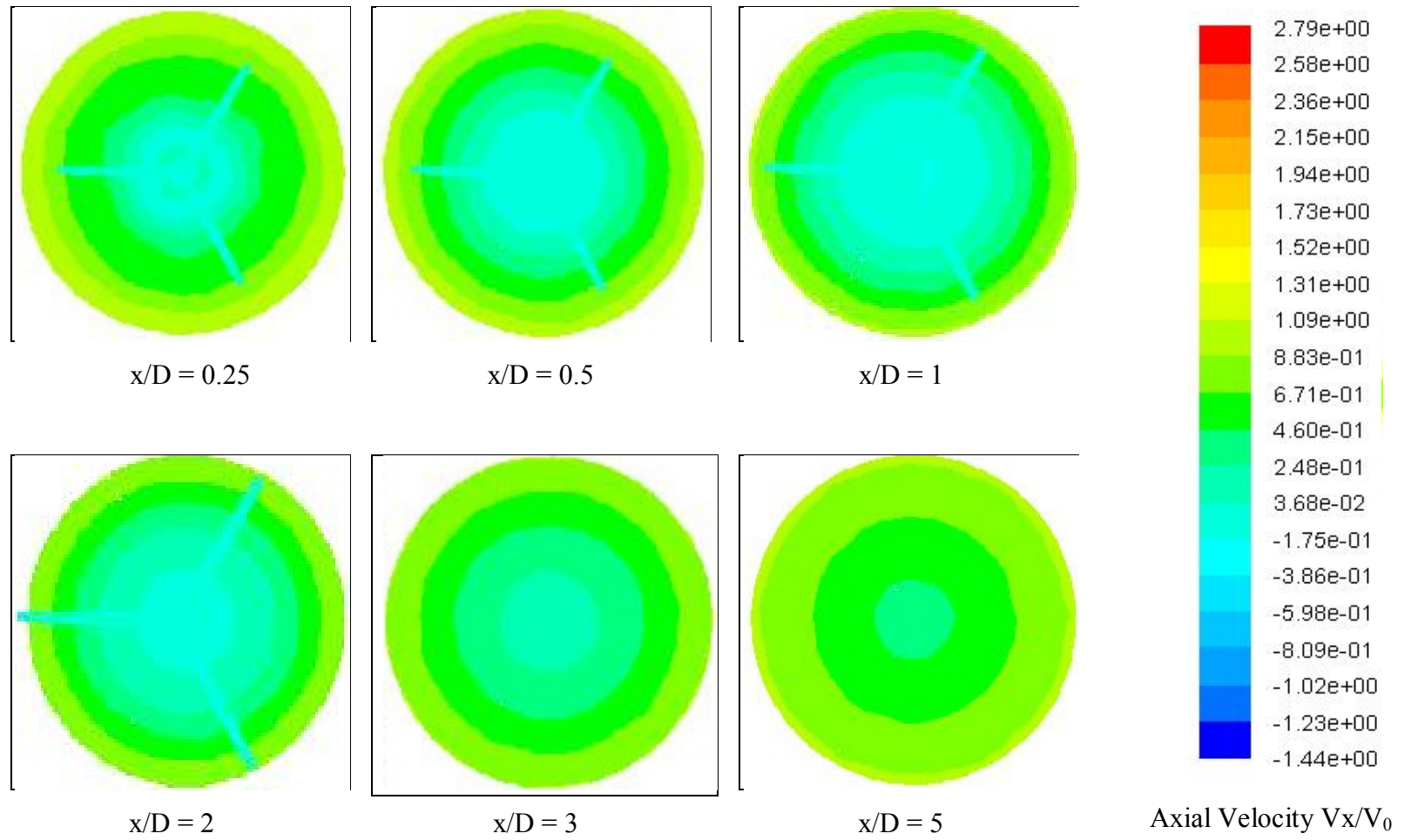


Figure 27. (b) Axial velocity contours at different x/D locations for TSR=7 with stream velocity $V_0=10$ m/s

Figure 28 shows the wake expansion along the flow at $y = 0$ inclined plane, which cuts through the turbine blade at angle of 60° to the z -axis

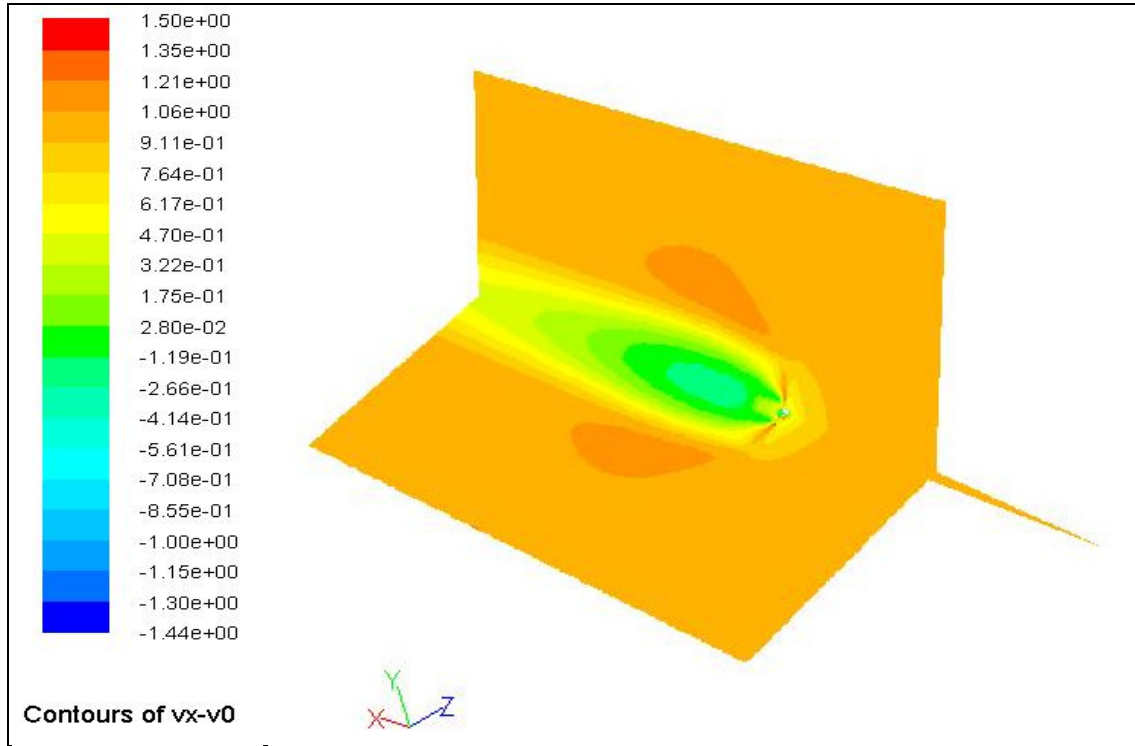


Figure 28. Axial velocity distributions along the flow direction

As flow moves downstream, it can be seen that wake expands along the direction of the flow. However, magnitude of velocity decreases within the stream tube. Green area right after the turbine indicates very low and even negative velocities caused by the hub bluntness and mixing flows. Light yellow area corresponds to velocity magnitude of about 6.17 m/s at the outflow, which kept at distance of $5D$ after the rotor. The wake field boundary shows a smoother gradient and the far wake is dominated by diffusion phenomena, so that the wake is forced by external flow.

It is of interest to know the turbulence characteristics in wind farms in order to predict the mechanical loads on the wind turbines and their performances and to evaluate the velocity deficit created in the wind stream by the drag of the turbines.

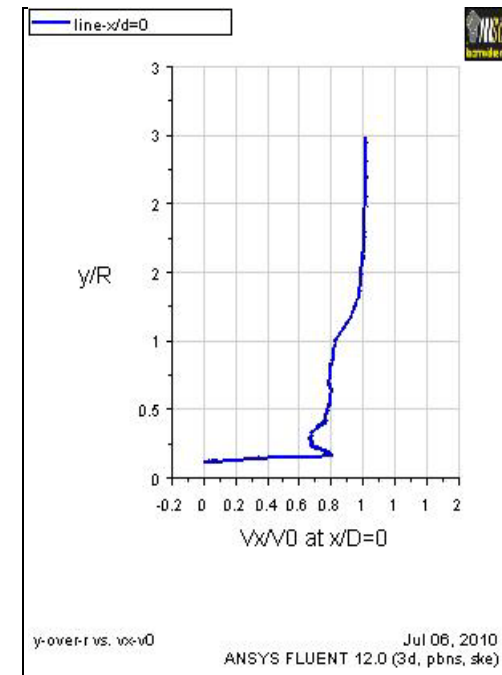
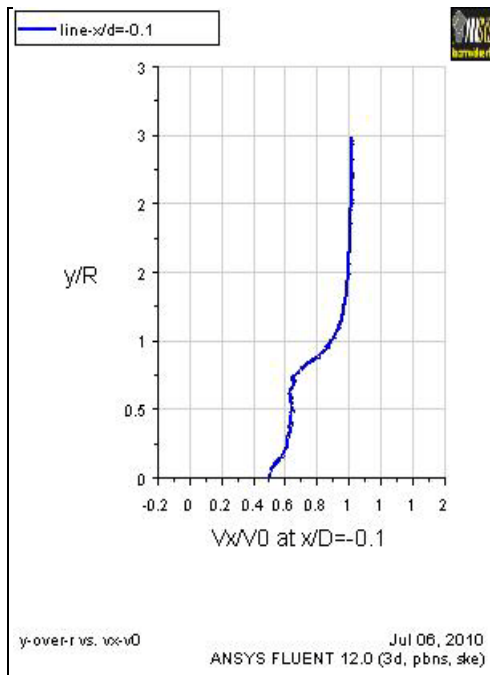
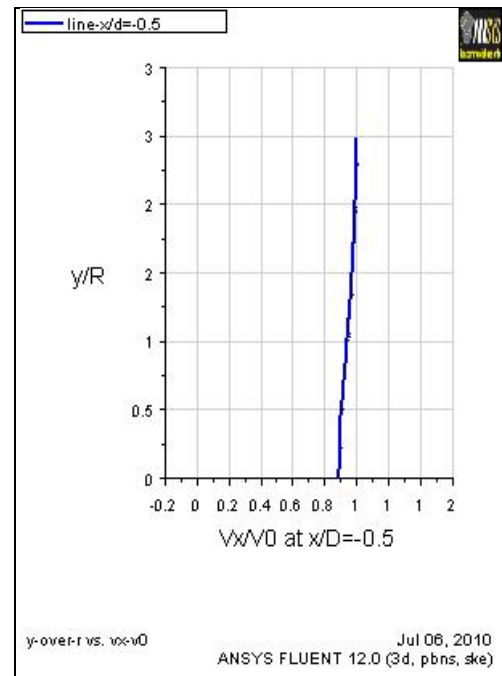
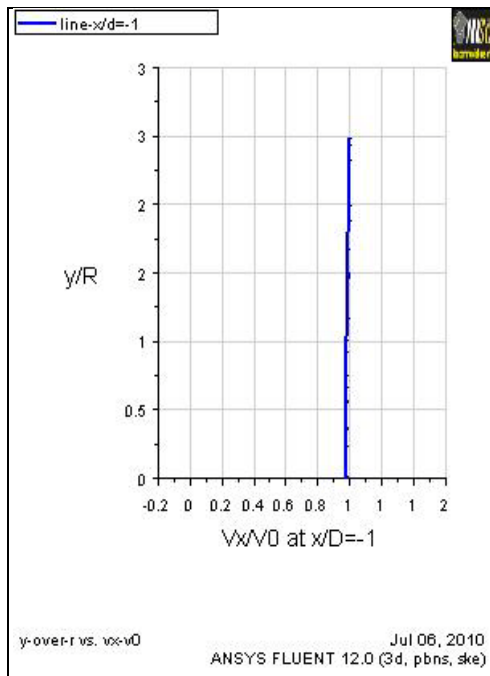
A distinct division can be made into near and far wake region.

- The near wake is taken as the region just behind the rotor, where the properties of the rotor flow can be noticeably discriminated, roughly up to one rotor diameter downstream. In this region the presence of the rotor is visible because of the aerodynamic perturbation created by the blades, including stalled flow, 3-D effects and tip vortices.

The near wake survey is focused on the physical process of energy conversion.

- Otherwise, the far wake is the region beyond the near wake, where the focus is put on the mutual influence of wind turbines in farm situations. The main research interest is to study how the far wake decays down-stream, in order to estimate the effects produced on the downstream turbines, i.e. lower velocity and higher turbulence intensity, which make the power production decrease and the unsteady loads increase.

This observation is helpful in means of positioning next turbine when wind farm considered and it is clear that 5D distances is not enough. More deep far wake studies are required for such determination.



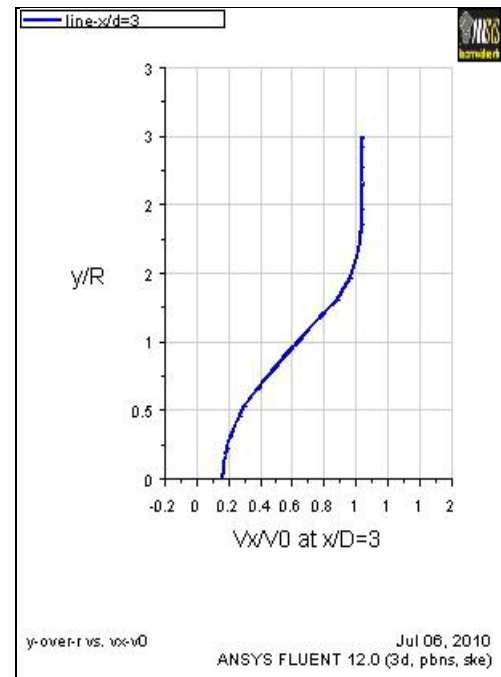
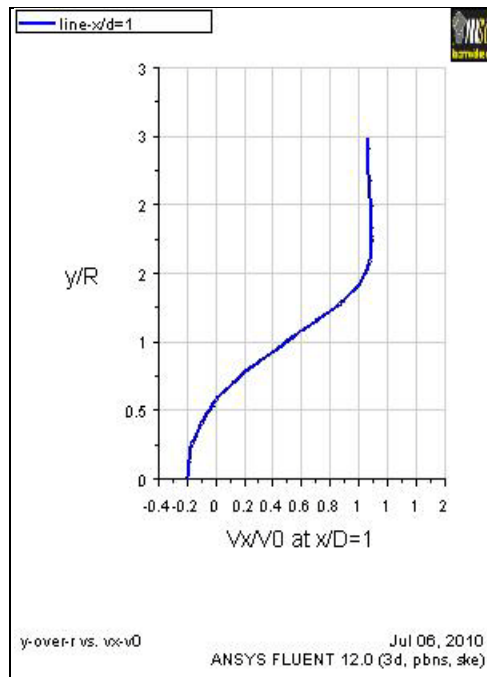
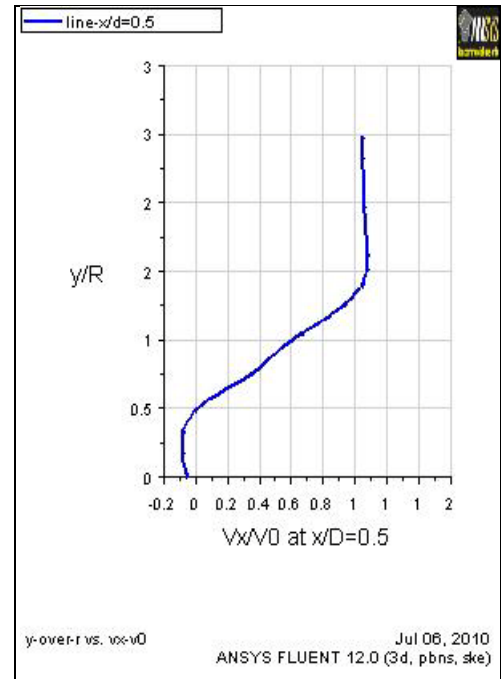
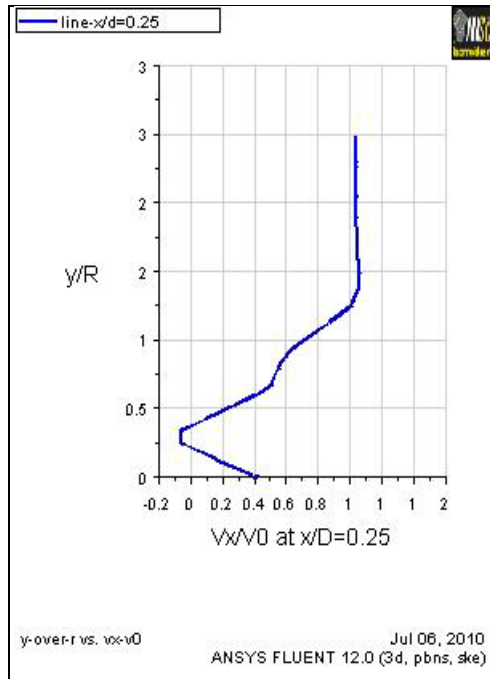


Figure 29. Axial velocity plots along the radial lines
at various x/D locations: V=10 m/s, TSR=7

Figure 29 shows the axial velocity plots at various x/D locations taken at radial lines inclined at the angle of 60° to the z -axis. Here also can be observed the fact that axial velocity gets reduced before the turbine and geometry of the hub (bluntness) also accounts for zero or sub-zero velocities downstream of the rotor. Negative velocities are present also due to mixing of the flow stream. The expansion of the wake can be visualized where velocity reaches the stream velocity V_0 and shifts further outward radially as the flow advances.

In addition, radial and tangential velocity contours are presented.

Figure 30 shows contours of radial velocities at various x/D locations. Contours are taken again from the center of the rotor's hub in radial direction at distance of 4m. Better visualization of near-blade region is obtained by creating clipped iso-surfaces. As expected, maximum variation of radial velocities is observed near the blade. At the tip of the blade there is significant increase of radial velocity. This is due to cross flows over the tip and rotation of the rotor itself. At about $x = 0.5D$ radial velocity is no longer affected. Upstream of the turbine disturbance starts at about $x=0.1D$. Close observation of the velocity gradients around the turbine shows that flow field is affected radially only at distance $r = 0.6D$ and no more.

Figure 31 shows contours of tangential velocities. As it can be observed from the contour plots, variations of tangential velocity vectors starts about at $x = -0.05D$ up to $x = 0.7D$.

Figure 32 depicts the plot of tangential velocity along the blade reaches the maximum value of -70 m/s at the tip. This agrees with theory, hence $\omega R = -70$ m/s. Negative sign indicates that tangential velocity acts in the opposite direction to the rotation.

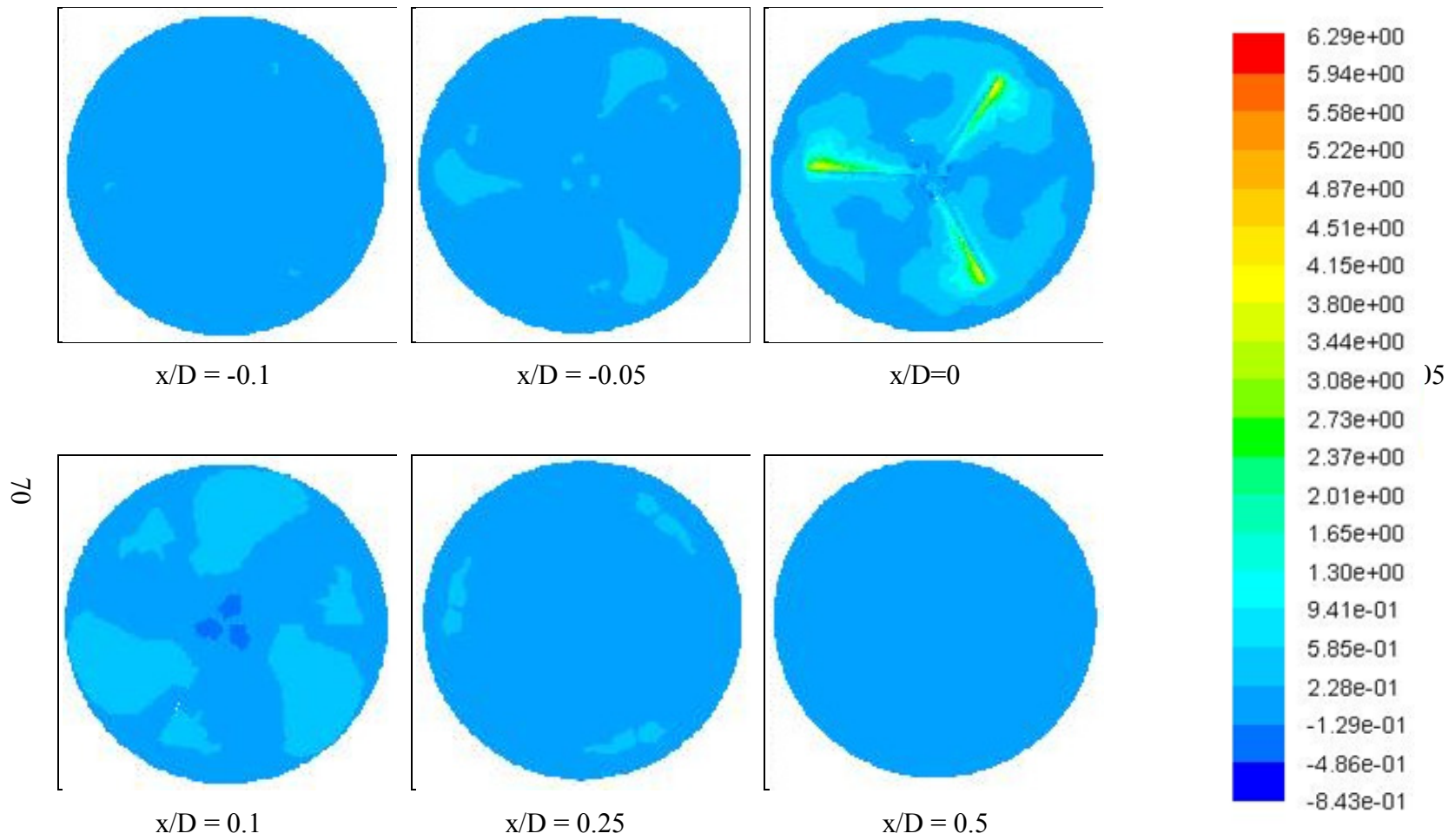


Figure 30. Radial velocity plots at different x/D locations with $V_0=10$ m/s and $TSR = 7$

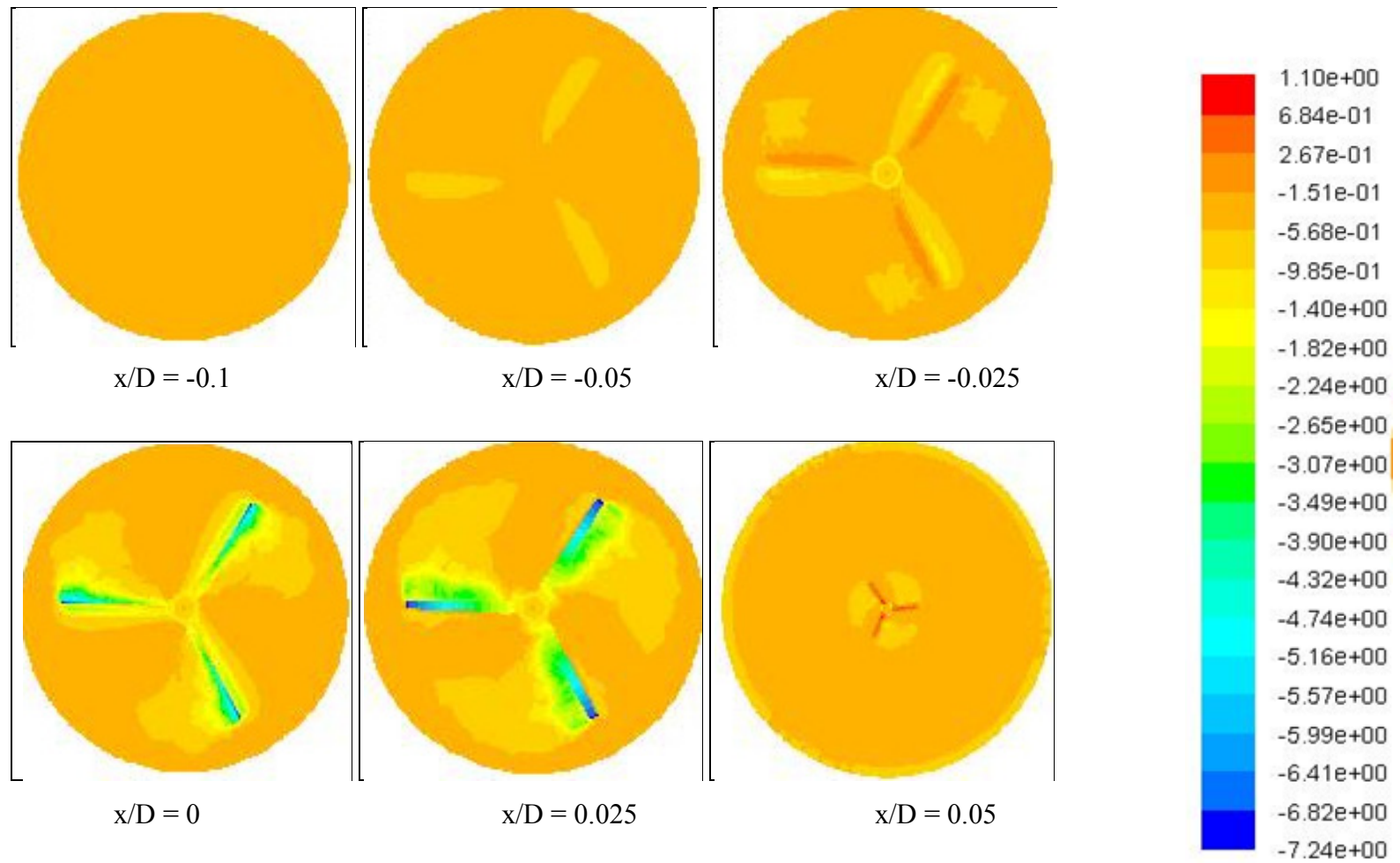
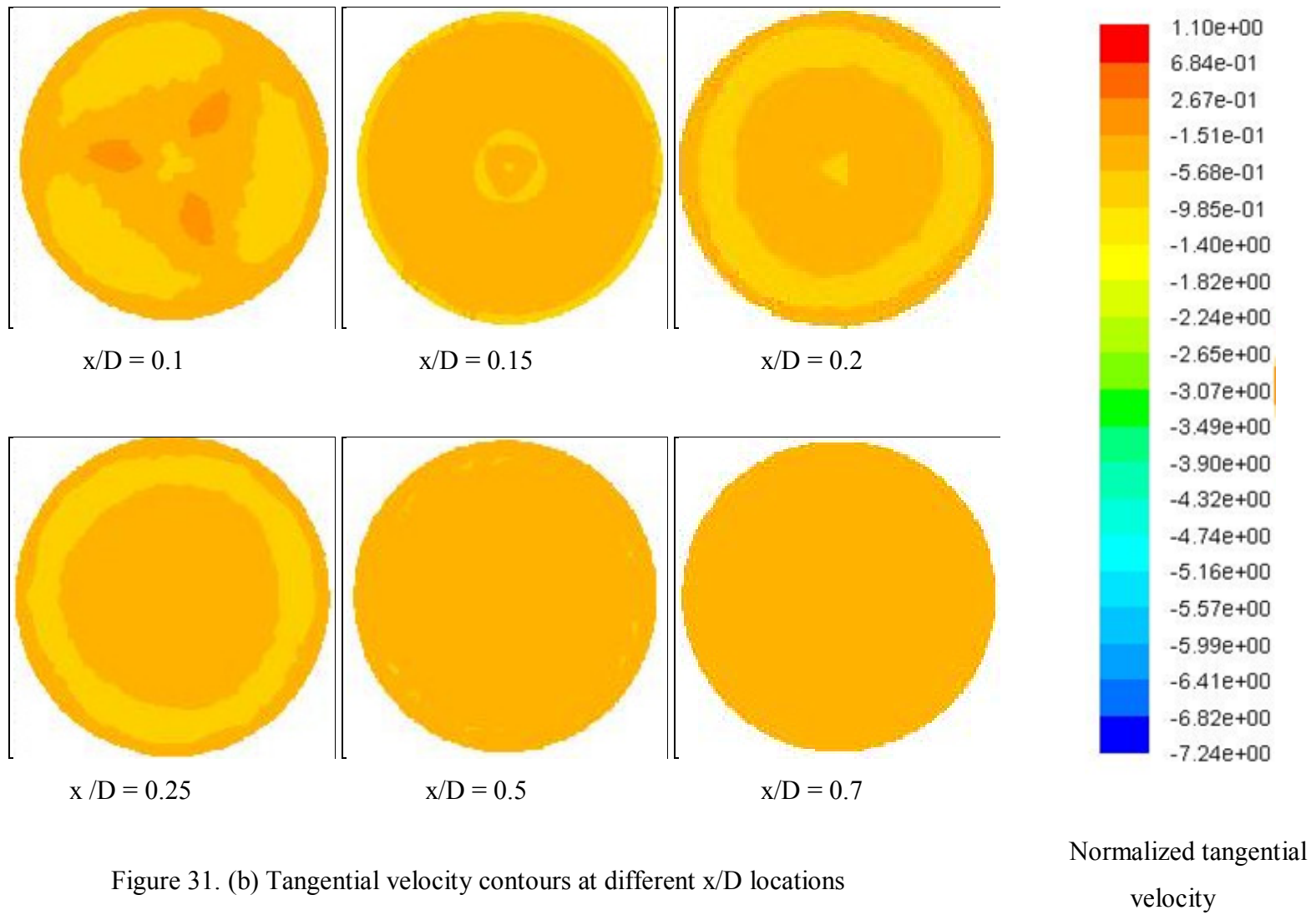


Figure 31. (a) Tangential velocity contours at different x/D locations

Normalized tangential
velocity



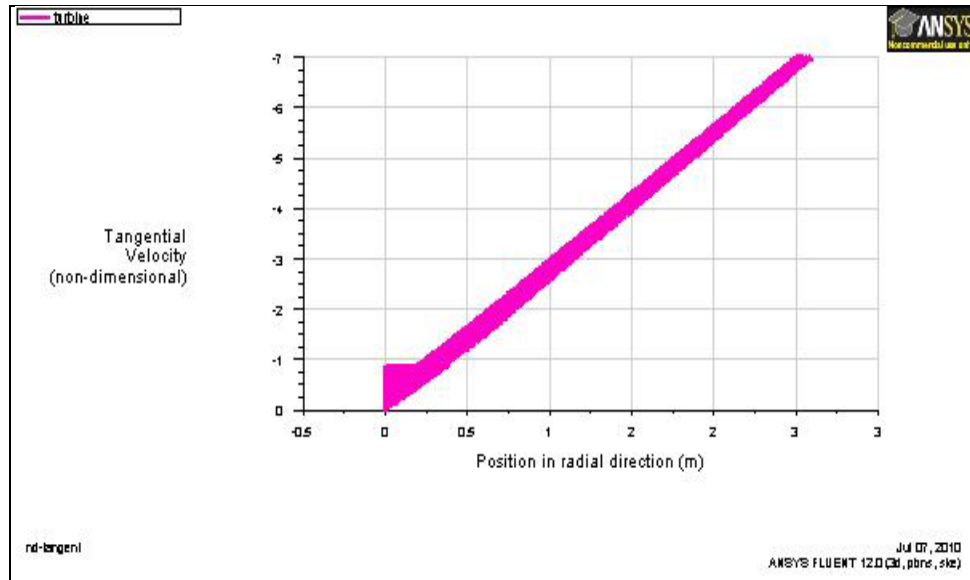


Figure 32. Tangential velocities along the blade

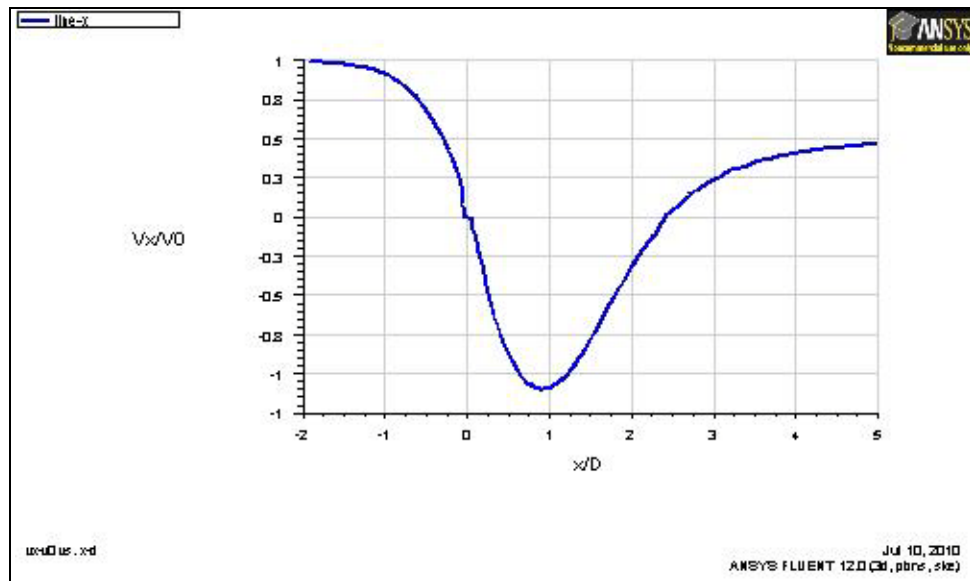


Figure 33. Axial velocities along the x-direction

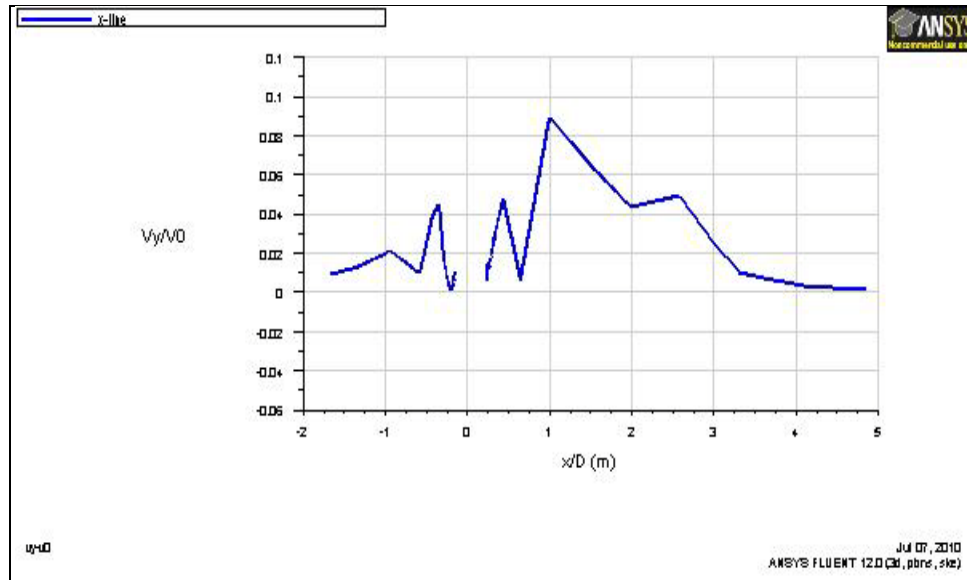


Figure 34. Radial velocities along the x- direction

Figure 33 shows the reduction of axial velocity along the flow direction. Check for velocity magnitude at the disk was done to confirm results with actuator disk theory and it is found in conformance with theory.

Figure 34 shows the radial velocity distribution along the flow direction. There are some jumps in magnitude around the turbine. This is expected in order to compensate the decrease along the flow direction.

Figure 35, given bellow, illustrates path-lines of particles released from the tip of the blade colored by velocity magnitude. Step size between the helixes is 0.5m.

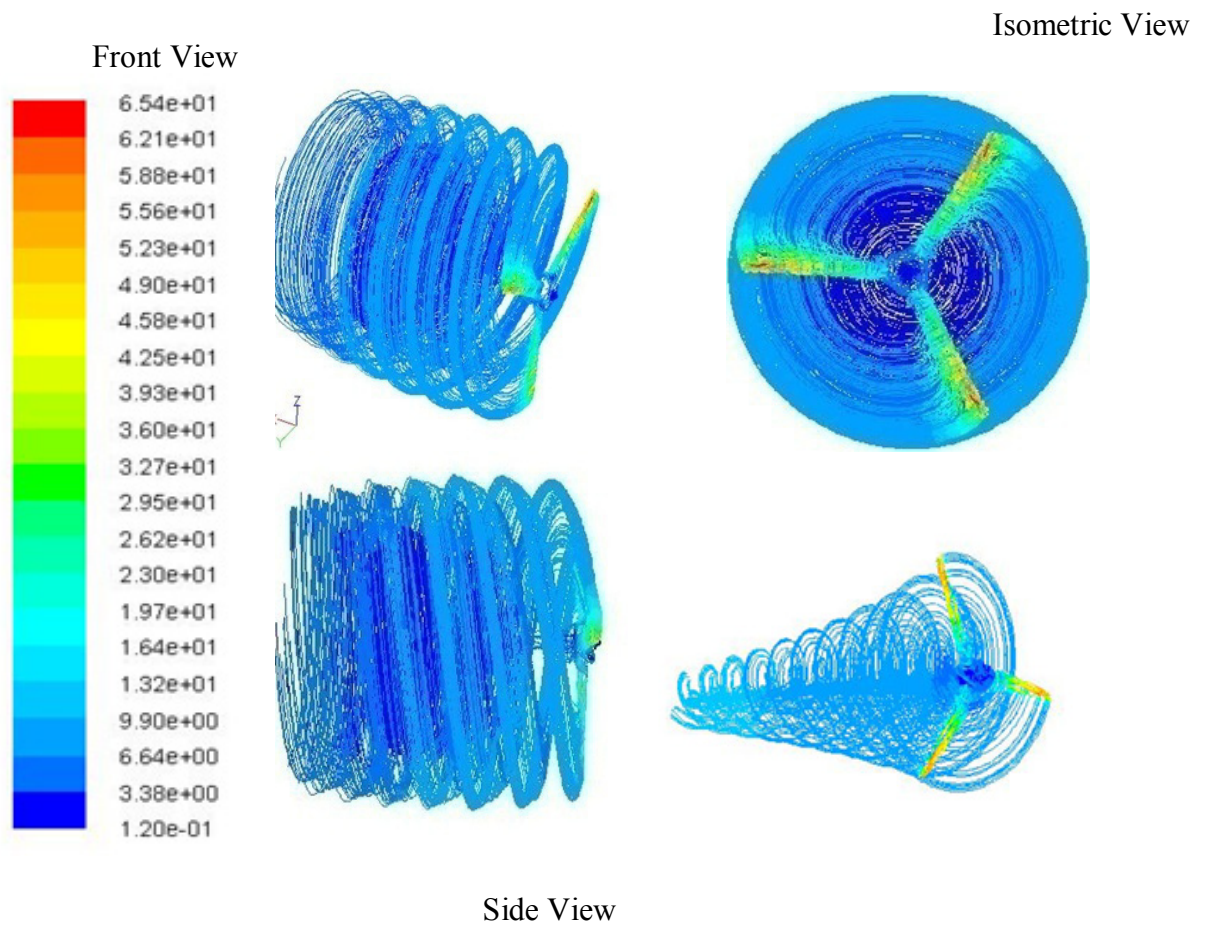


Figure 35. Pathlines colored by velocity magnitude

Pressure distribution along the flow direction is shown bellow in Figure 36. Graph is in conformance with actuator disk theory. As flow reaches the blade pressure increases and at the impact with the rotor pressure experiences drastic drop, reaches almost zero and after the blade it starts rising again. At about distance of 3D static pressure begin to stabilize and in ideal case reaches the undisturbed atmospheric pressure.

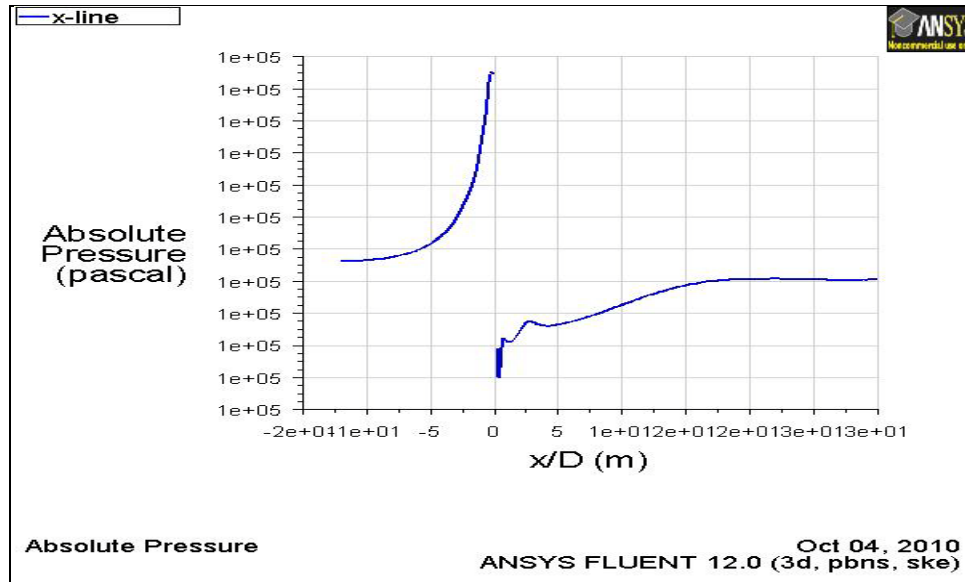


Figure 36. Static pressure distributions along the flow direction

There are many studies done for determination of pressure coefficient on the 2D section of airfoil at different x/chord locations. This study does not include such analysis; hence that requires enhanced wall treatment at boundary layer with $k-\omega$ SST turbulent model.

Turbulent viscosity contour is presented in Figure 37. The eddy viscosity ratio $\frac{\mu_t}{\mu}$ is the ratio between the turbulent viscosity, μ_t and the molecular dynamic viscosity, μ .

Eddy viscosity ratio is often also called turbulent viscosity ratio or simply viscosity ratio.

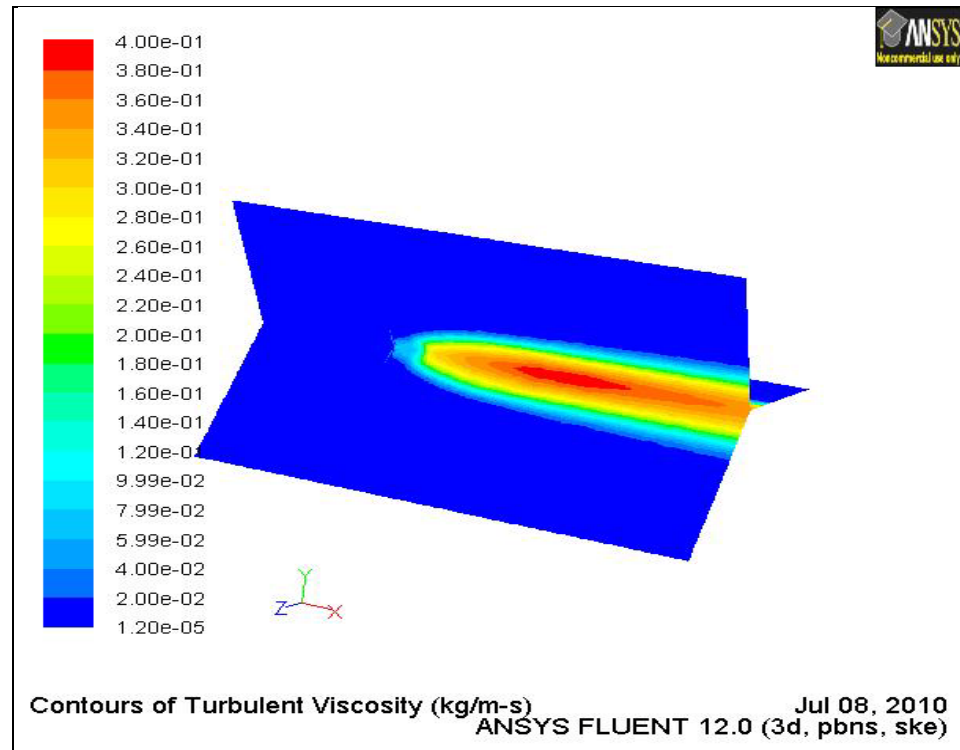


Figure 37. Turbulent viscosity contours, TSR=7, $V_0=10$ m/s

Turbulent viscosity increases in magnitude along the wake of the turbine. In order to find maximum distance that viscosity can reach, more extended domain in x-direction required. Similarly contours of turbulence intensity are plotted and presented in the Figure 38 bellow. The higher the intensity value, the more is the dominance of turbulence, that is, the more the dominance of dynamic random loads over the deterministic steady loads due to mean wind speed \bar{V} . Typically, turbulence intensity is in a range from 0.1 to 0.4.

By observation of the contours and plot in Figures 38 and 40 it can be seen that intensity reaches the value of about 25-30% (10% was specified at pre-processing phase) and then stabilizes to the original entered conditions.

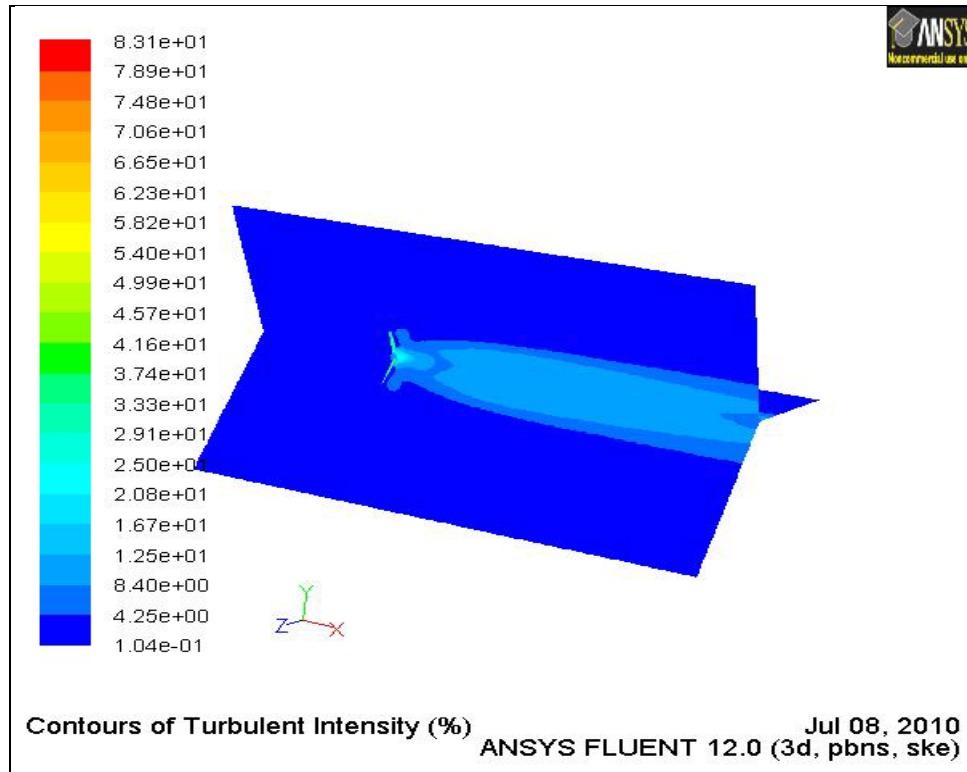


Figure 38. Turbulence intensity contours, $TSR = 7$, $V_0 = 10\text{m/s}$

Figures 39 and 40 are showing the plots of turbulent viscosity and intensity respectively.

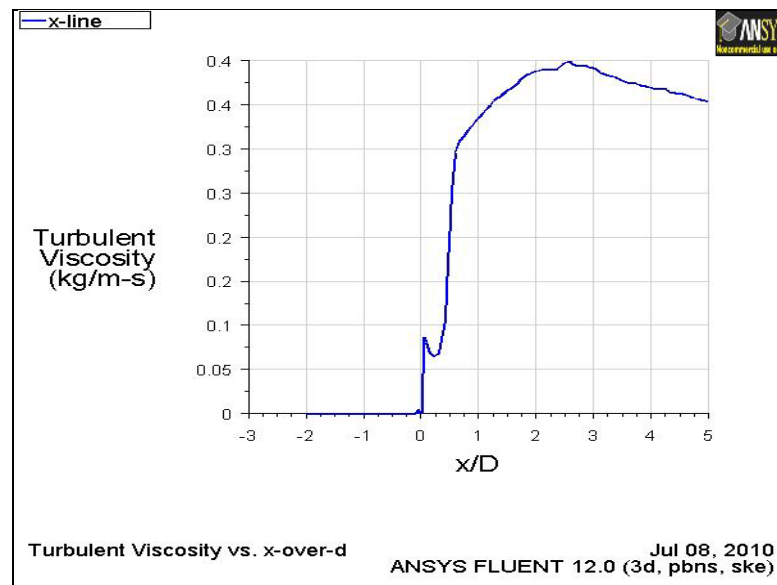


Figure 39. Turbulent viscosity plots at different x/D locations

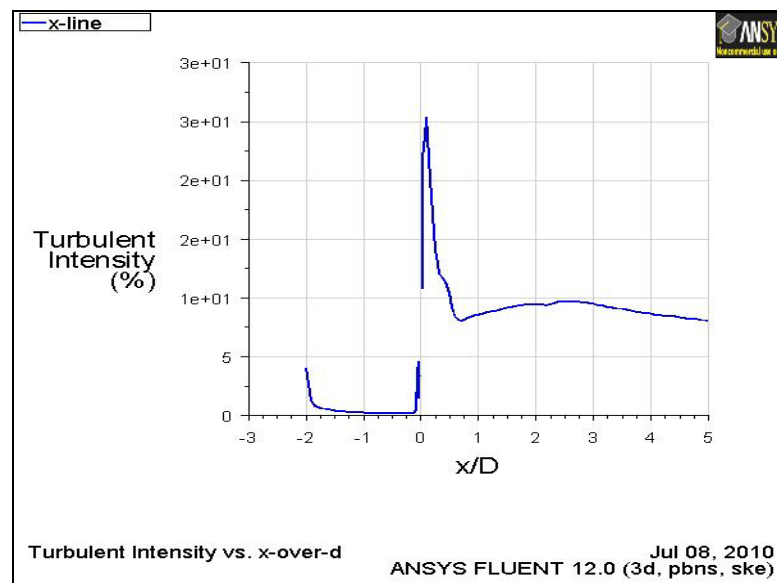


Figure 40. Turbulent intensity plots at different x/D locations

7.2 Parametric Studies

Parametric studies were performed for current CFD analysis. Cases were run under different conditions. First, rotational speed was kept constant at $\omega = 7.53$ rad/s (72 rpm) and stream velocity was changed from 4 m/s to 25 m/s. Secondly, flow velocity was kept at $V_0 = 10$ m/s and rotational speed varied from 10 rad/s to 30 rad/s.

Table 3, given below, contains the calculated values for available, theoretical and actual power. Last column in the table represents the efficiency of the simulated turbine.

The following explains the difference between three power definitions: available power is the power available in the wind; the theoretical power is the maximum possible power that turbine could extract under ideal conditions. This can be obtained when multiplying the available power by maximum theoretical efficiency $C_{p_{max}} = 0.59$ (Betz limit). Finally, the actual power of the turbine is the power obtained, when actual efficiency at different wind speeds are used.

Wind Speed m/s	Available Power, Kw	Theoretical Power, Kw	Actual Power, Kw	Efficiency, Cp
4	1.11	0.66	0.36	0.32
5	2.16	1.28	1.05	0.48
7	5.94	3.52	1.74	0.29
8	8.87	5.25	2.16	0.24
10	17.32	10.25	3.65	0.21
12	29.93	17.72	4.45	0.15
20	138.54	82.02	16.62	0.12
25	270.59	160.19	22.78	0.08

Table 3. Power output at different wind speeds

Figure 41 depicts the power outputs (Kw) versus wind speeds (m/s) for actual, theoretical and available power. As it was expected the theoretical maximum power is less than available power in the wind by factor of 0.59 and bottom curve of the plot represents the actual power, produced by the turbine under this simulated wind conditions.

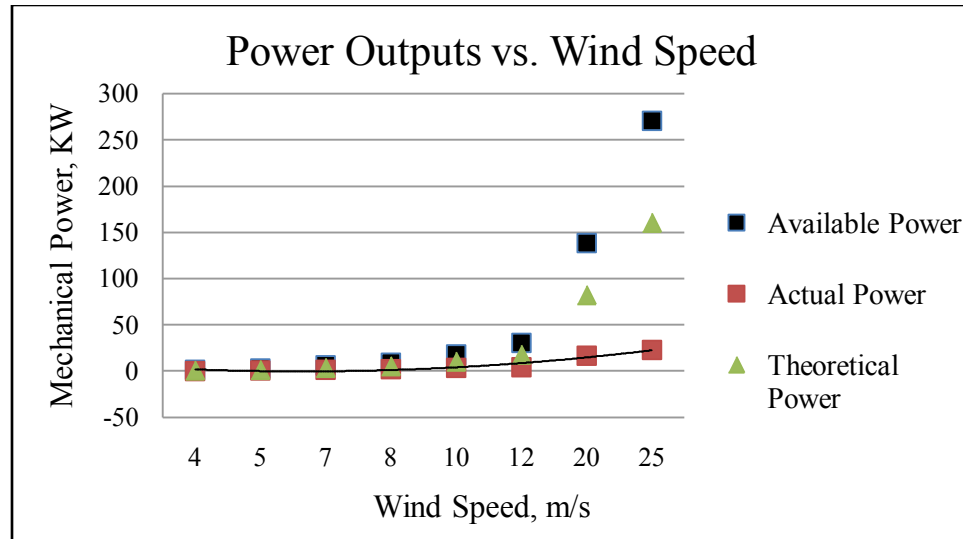


Figure 41. Power outputs vs. wind speed, $\omega=7.53$ rad/s

Given below in Figure 42, is the turbine's efficiency plotted against the same wind conditions. As it can be observed, the maximum efficiency of 48% is obtained at wind speed of 5 m/s. As wind speed increases the efficiency of the turbine decreases. Such observations will help to predict the rated operational wind conditions for the designed turbine. So, it can be noted that the rated wind speed of the simulated turbine is around 5 m/s and at that wind speed the turbine reaches its maximum efficiency.

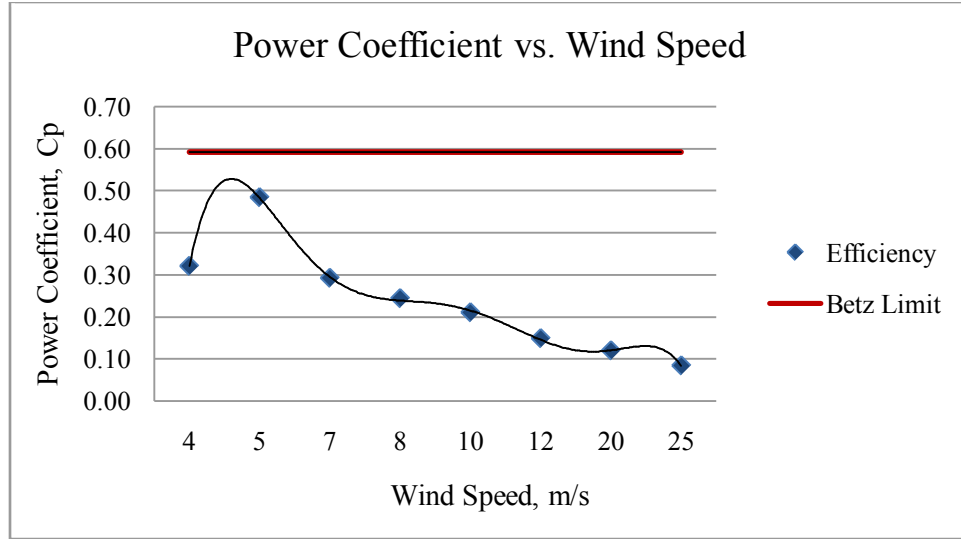


Figure 42. Power coefficient (efficiency) vs. wind speed, $\omega=7.53$ rad/s

Table 4 shows the calculated power and efficiency for different TSR's at constant wind speed of 10 m/s. Table also shows the values for the rotational torque and pressure coefficient along the flow direction. In Figure 43, power versus TSR is presented. As it was described earlier, maximum shaft power (7Kw) is registered at TSR=7.

Tip speed ratio, λ	Rotational speed, rad/s	Total Moment (Torque), N-m	Pressure Coefficient	Power Coefficient	Actual Power, Kw
3	10.00	200.20	3.32	0.14	2.55
4	13.33	305.50	4.98	0.27	4.83
5	16.66	412.45	6.72	0.37	6.43
6	20.00	461.89	7.54	0.36	6.34
7	23.33	540.72	8.82	0.40	6.93
8	26.66	631.06	10.30	0.37	6.38
9	30.00	760.56	12.41	0.32	5.61

Table 4. Turbine's characteristic parameters at different TSR, $V_0=10$ m/s

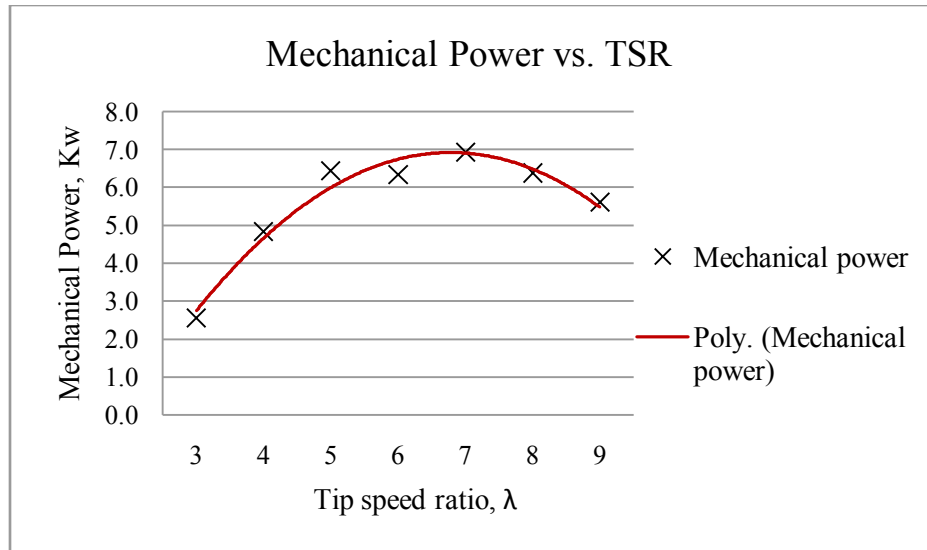


Figure 43. Mechanical power at different TSR, $V_0=10$ m/s

CONCLUSION

In this research work, a generic study of a flow field around horizontal axis wind turbine was investigated using RANS method. The model has been validated against the results of a Phase VI rotor experiment conducted by NREL. The turbine power coefficient obtained in this study using CFD analysis was in good agreement with experimental data. Near and far wake studies have been carried out. The variations of the velocity components, axial, radial and tangential have been investigated and presented. The reduction in axial flow velocity profiles as the flow moves along is in agreement with actuator disk theory. Axial, radial and tangential velocity contours at different x/D locations are presented. It was found out that tangential velocity effects decays faster than the radial velocity effects. Parametric study was also performed to investigate the turbines power at different free stream wind velocities. Turbines power increases as wind speed increases; however, at low speeds the predictions are underestimated. Pressure distribution, the turbulent viscosity and turbulent intensity plots were also presented.

The future work is recommended to:

- Investigate the pressure distribution on the blade surface by performing 2D analysis of the airfoil section.
- Predict lift and drag coefficients at different angles of attack.

- Use more sophisticated meshing techniques to create structured mesh with hexahedral elements and achieve refinement of boundary layer by keeping y^+ resolution around 1.
- Use other turbulence models such as $k-\omega$ SST and Spalart-Almaras
- Use Large Eddy Simulation and Detached Eddy Simulation methods for the visualization of the temporal evolution of large vortices.

APPENDIX A

Actuator Disc Theory

The Actuator disc model is probably the oldest analytical tool for evaluating rotor performance. The model is based on conservation of mass, momentum and energy, and constitutes the main ingredient in the 1D momentum theory. Method fits very well with current studies and it is presented bellow.

The rotor is represented by an “actuator disc” that creates a pressure discontinuity of area A and undisturbed velocity V [28, 29]. The control volume of the model is defined by a stream tube whose fluid passes through the rotor disk. The wind at the inlet has an approach velocity V_0 over an area A_0 , and a slower downstream velocity V_3 over a larger area A_3 at the outlet. A simple schematic of the model is given in Figure 44.

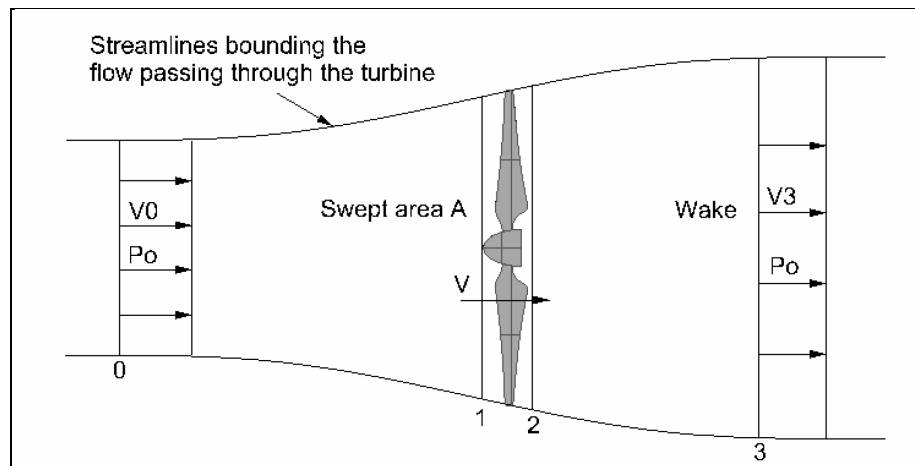


Figure 44. Control Volume for the idealized actuator-disk analysis

The actuator disc approach uses the following assumptions:

- The flow is ideal and rectilinear across the turbine i.e. steady, homogenous, inviscid, non-rotational, and incompressible. Both the flow and thrust are uniform across the disk.
- Infinite number of blades
- Non rotating wake
- The static pressure at the upwind and downwind boundaries is equal to the ambient static pressure.

By applying a horizontal momentum relation between sections 0 and 3 the thrust at the rotor disk can be found:

$$\sum F_x = -T = \dot{m}(V_0 - V_3) = \rho AV(V_0 - V_3) \quad [1]$$

Where, ρ is the fluid density, A the area of cross-section of the actuator disk and U_1 and U_3 are the inflow and outflow velocity respectively. For a steady state flow ρAV_1 and ρAV_2 can be replaced by \dot{m} , where \dot{m} is the mass flow rate. Then thrust becomes

$$T = \dot{m}(V_1 - V_2) \quad [2]$$

Across the disk the velocity is assumed to be same.

Applying Bernoulli function in the two control volumes

Upstream:

$$p_1 + \frac{1}{2}\rho V_1^2 = p_{21} + \frac{1}{2}\rho V_2^2 \quad [3]$$

Downstream

$$p_{23} + \frac{1}{2}\rho V_2^2 = p_3 + \frac{1}{2}\rho V_3^2 \quad [4]$$

Where, p_{21} and p_{23} are pressure on the right and left side of the disk respectively.

Pressures at far field p_1 and p_3 are equal.

The thrust can be expressed as the net sum of the forces on each side of the actuator disk:

$$T = \frac{1}{2} \rho A (V_1^2 - V_3^2) \quad [5]$$

Where, A is the actuator disk area.

The thrust values from equation [2] and [5] when combined gives

$$V = \frac{1}{2} (V_0 + V_3) \quad [6]$$

Where, V is the stream velocity at the turbine.

The power output, is equal to thrust times the velocity at the disk

$$P = \frac{1}{2} \rho A (V_1^2 - V_3^2) \cdot \left(\frac{V_1 + V_3}{2} \right) \quad [7]$$

$$P = \frac{1}{4} \rho A V_1^3 \cdot \left(1 - \frac{V_3^2}{V_1^2} \right) \left(1 + \frac{V_3}{V_1} \right) \quad [8]$$

Substituting $\frac{V_3}{V_1}$ with x and equating first derivative to zero, maximum power can be

obtained

$$\frac{d}{dx} (1 - x^2) (1 + x) = 0 \quad [9]$$

$$3x^2 + 2x - 1 = 0 \quad [10]$$

From the above quadratic equation, $x = \frac{1}{3}$

Substituting for x in equation [8],

$$P_{\max} = \frac{1}{4} \rho A V_1^3 \cdot \left(1 - \frac{1}{9}\right) \left(1 + \frac{1}{3}\right) \quad [11]$$

$$P_{\max} = \frac{16}{27} \cdot \frac{1}{2} \rho A V_1^3 \quad [12]$$

The coefficient of power C_p is defined by

$$C_p = \frac{\text{Rotor Power}}{\text{Power in the wind}} \quad [13]$$

Hence,

$$C_p = \frac{16}{27} = 0.5926 \quad [14]$$

This is called that Betz Limit. It is the theoretical maximum possible power coefficient.

REFERENCES

- [1] World Wind Energy Association (WWEA), World Wind Energy Report 2009
<http://www.wwindea.org>
- [2] World Energy Outlook 2009
<http://www.iea.org>
- [3] Vermeer LJ, Sørensen JN, Crespo A. Wind Turbine Wake Aerodynamics; *Progress in Aerospace Science*, 2003; Vol. 39; 467-510.
- [4] Sørensen JN, Shen WZ. Numerical Modeling of Wind turbine Wakes; *J. Fluid Engineering* 2002; Vol.124; 393-399.
- [5] Ivanell SSA. *Numerical computations of wind turbine wakes*; Technical reports from KTH Mechanics, Royal Institute of Technology; Stockholm, Sweden; 2005.
- [6] Kang S, Hirsch C. Features of the 3D flow around wind turbine blades based on numerical solutions; *Proceedings from EWECE* 2001, Copenhagen.
- [7] Alinot C, Masson C. Aerodynamic simulation of wind turbines operating in atmospheric boundary layer with various thermal stratifications; *AIAA Paper* 2002-0042.
- [8] Mikkelsen R. *Actuator disc methods applied to wind turbines*; Dissertation submitted to the Technical University of Denmark in partial fulfillment of the requirements for the degree of PhD in Mechanical Engineering; Lyngby, 2003.
- [9] Xu G, Sankar LN. Computational study of HAWT; *AIAA Paper* 1999-0042.
- [10] Xu G, Sankar LN. Effects of transition, turbulence and yaw on the performance of HAWT; *AIAA Paper* 2000-0048.
- [11] Benjanirat S, Sankar LN, Xu G. Evaluation of turbulence models for the prediction of wind turbine aerodynamics; *AIAA Paper* 2003-0517.

- [12] Duque EPN, Van Dam CP, Hughes S. Navier-Stokes simulations of the NREL combined experiment phase II rotor. AIAA Paper 99-0037, 1999.
- [13] Ekaterinaris JA. Numerical simulation of incompressible two-bladed rotor flow field. AIAA Paper 97-0398, 1997.
- [14] Sørensen NN, Michelsen JA. Aerodynamic predictions for the unsteady aerodynamics experiment phase-II rotor at the National Renewable Energy Laboratory. *AIAA Paper 2000-0037*, 2000.
- [15] Michelsen JA, Sørensen NN. Current developments in Navier-Stokes modeling of wind turbine rotor flow; *Proceedings from EWECC 2001*, Copenhagen.
- [16] Sørensen NN. 3-D Background aerodynamics using CFD; *Risø National Laboratory*, Roskilde, Denmark, 2002.
- [17] Sørensen NN, Johansen J, Conway S. KNOW-BLADE Task-3.1 report. Computations of wind turbines blade loads during standstill operation. *Risø National Laboratory*, Roskilde, Denmark, 2004.
- [18] Sørensen NN, Johansen J, Conway S, Voutsinas S, Hansen MOL, Stürmer A. KNOW-BLADE Task-3.2 report. Tip Shape Study. *Risø National Laboratory*, Roskilde, Denmark, 2005.
- [19] Mandas N, Carcangiu CE, Cambuli F. The economy of large scale wind turbines; *Fluent News* Summer 2005; Vol. XV; 5-7.
- [20] NASA, Turbulence modeling resource:"The Menter Shear Stress Transport Turbulence Model". <http://turbmodels.larc.nasa.gov/sst.html>
- [21] Kuik, G.A.M., *the Lanchester-Betz-Joukowski Limit*, Wind Energy 10, 2007, 10pp. 289-291
- [22] Jonkman, J.M., 2003, "Modeling of the UEA Wind Turbine for Refinement of FAST_AD," Technical report for the National Renewable Energy Laboratory, TP-500-34755
- [23] White, F.M., 1988, *Fluid Mechanics*, 2nd Edition, McGraw-Hill, Singapore
- [24] David Hartwanger, and Dr Andrej Horvat," 3D MODELING OF A WIND TURBINE USING CFD", NAFEMS Conference 2008, United Kingdom
- [25] Glauert, H., Aerodynamic Theory, Vol. 4, Berlin, Germany, Julius Springer, 1935: p. 169 – 360

- [26] "Bernoulli's equation". NASA Glenn Research Center.
<http://www.nasa.gov/WWW/K-12/airplane/bern.htm>. Retrieved 2009-03-04.
- [27] Spalart P. R. and Allmaras S. R. A one equation turbulence model for aerodynamic flows. In AIAA 92-0439, AIAA 30th Aerospace Sciences Meeting and Exhibit, Reno, NV, January 1992.
- [28] Jonkman, J.M., 2003, "Modeling of the UEA Wind Turbine for Refinement of FAST_AD," Technical report for the National Renewable Energy Laboratory, TP-500-34755
- [29] White, F.M., 1988, *Fluid Mechanics*, 2nd Edition, McGraw-Hill, Singapore
- [30] Anderson, J.D.Jr., Computational Fluid Dynamics – The basics with Applications, McGraw-Hill, 1995
- [31] Fluent, *ANSYS FLUENT 12.0 Theory Guide*, ANSYS Inc., April 2009, Sections 18.1.1 and 18.1.2
- [32] Fluent, *ANSYS FLUENT 12.0*, Tutorial 9-11-12-23-28-29. Turbulence and Discrete Phase Modeling.
- [33] Launder, B.E. and Spalding, D.B., *Lectures in Mathematical Models of turbulence*, Academic Press, London, England, 1972
- [34] Bahaj, A.S., Batten, W.M.J., Molland, A.F., Chaplin, J.R.. *Power and thrust measurement of marine current turbines under various hydrodynamic flow*
- [35] Cmltech, "CFD Grid Generation Methods"
http://www.chmltech.com/cfd/grid_generation.pdf
- [36] Acker, T.; Hand, M., "Aerodynamic Performance of the NREL Unsteady Aerodynamics Experiment (Phase IV) Twisted Rotor", AIAA-99-0045, Prepared for the 37th AIAA Aerospace Sciences Meeting and Exhibit, Reno, NV, January 11-14, 1999, p. 211-221.
- [36] Sorensen J.N. and Shen W.Z. Numerical modeling of wind turbine wakes. *Journal of Fluid Engineering*, 124:393–9, 2002.
- [37] Madsen, P. H.; Pierce, K.; Buhl, M., "Predicting Ultimate Loads for Wind Turbines", AIAA-99-0069, Prepared for the 37th AIAA Aerospace Sciences Meeting and Exhibit, Reno, NV, January 11-14, 1999, p. 355-364.

- [38] Xu, G.; Sankar, L. N., "Computational Study of Horizontal Axis Wind Turbines", AIAA-99-0042, Prepared for the 37th AIAA Aerospace Sciences Meeting and Exhibit, Reno, NV, January 11-14, 1999, p. 192-199.
- [39] Giguère, P. and Selig, M.S., "Design of a Tapered and Twisted Blade for the NREL Combined Experiment Rotor," NREL Subcontract Report, NREL/SR-500-26173.
- [40] Jonkman, J.M., 2003, "Modeling of the UEA Wind Turbine for Refinement of FAST_AD," Technical report for the National Renewable Energy Laboratory, TP-500-34755
- [41] Hau E. Wind turbines. Springer: Berlin, 2000.
www.loc.gov › Researchers
- [42] Fluent 12.0, Tutorial 9-11-12-23-28-29. Turbulence and Discrete Phase Models Wilcox C. D., (1998), "Turbulence Modeling for CFD" 2nd Ed., (DWC Industries, La Canada)
- [43] Simms, D., Schreck, S., Hand, M., and Fingersh, L.J., 2001, "NREL Unsteady Aerodynamics Experiment in the NASA-Ames Wind Tunnel: A Comparison of Predictions to Measurements," Technical report for the National Renewable Energy Laboratory, TP-500-29494
- [44] Bardina, J. E., Huang, P. G. and Coakley, T.J., "Turbulence Modeling Validation, Testing, and Development," *NASA Technical Memorandum* 110446, April 1997
- [45] Versteeg H.K. and Malalasakera W. An Introduction to Computational Fluid Dynamics: The Finite-Volume Method. Harlow: Longman Scientific & Technical: New York, 1995.
- [46] Ferziger J.H. and Peric M. Computational Methods for Fluid Dynamics. Springer-Verlag: Berlin, 1999.
- [47] Gary L. Johnson "Wind Energy Systems" second edition, 2006
eece.ksu.edu/~gjohnson/Windbook.pdf